EUROPEAN ORGANIZATION FOR NUCLEAR RESEARCH

Non-linear flow modes of identified particles in Pb–Pb collisions at $\sqrt{s_{\mathrm{NN}}} = 5.02$ TeV

ALICE Collaboration*

Abstract

The p_{T}-differential non-linear flow modes, $v_{4,22}$, $v_{5,32}$, $v_{6,33}$ and $v_{6,222}$ for $\pi^{\pm}$, $K^{\pm}$, K^0_S, $p+\overline{p}$, $\Lambda+\overline{\Lambda}$ and ϕ-meson have been measured for the first time in Pb–Pb collisions at $\sqrt{s_{\mathrm{NN}}} = 5.02$ TeV with the ALICE detector at the Large Hadron Collider. The results were obtained with a multi-particle technique, correlating the identified hadrons with reference charged particles from a different pseudorapidity region. These non-linear observables probe the contribution from the second and third order initial spatial anisotropy coefficients to higher flow harmonics. All the characteristic features observed in previous p_{T}-differential anisotropic flow measurements for various particle species are also present in the non-linear flow modes, i.e. increase of magnitude with increasing centrality percentile, mass ordering at low p_{T} and particle type grouping in the intermediate p_{T} range. Hydrodynamical calculations (iEBE-VISHNU) that use different initial conditions and values of shear and bulk viscosity to entropy density ratios are confronted with the data at low transverse momenta. These calculations exhibit a better agreement with the anisotropic flow coefficients than the non-linear flow modes. These observations indicate that non-linear flow modes can provide additional discriminatory power in the study of initial conditions as well as new stringent constraints to hydrodynamical calculations.

---

*See Appendix B for the list of collaboration members

Contents

1 Introduction

Lattice quantum chromodynamics (QCD) calculations [1, 2] suggest that at extremely high temperature and energy density a state of matter is produced in which quarks and gluons are no longer confined into hadrons. This state of matter is called the quark-gluon plasma (QGP) [3–5]. The main goal of heavy-ion collision experiments is to study the properties of the QGP, such as the speed of the sound, the equation of state and its shear and bulk viscosities.

One of the observables sensitive to these properties is the azimuthal angular distribution of particles emitted in the plane perpendicular to the beam axis. In a heavy ion collision, the overlap region of the colliding nuclei exhibits an irregular shape [6–12]. This spatial irregularity is a superposition of the geometry, i.e. centrality of the collision reflected in the value of the impact parameter, and the initial energy density in the transverse plane which fluctuates from event to event. Through interactions between partons and at later stages between the produced particles, this spatial irregularity is transferred into an anisotropy in momentum space. The latter is usually expressed by a Fourier expansion of the azimuthal particle distribution [13] according to

$$\frac{\mathrm{d}N}{d\varphi} \propto 1 + 2\sum_{n=1}^{\infty} v_n(p_{\mathrm{T}})\cos[n(\varphi - \Psi_n)], \tag{1}$$

where N, p_{T} and φ are the particle yield, transverse momentum and azimuthal angle of particles, respectively, and Ψ_n is the azimuthal angle of the nth-order symmetry plane [7–10, 12]. The coefficient v_n is the magnitude of the nth-order complex flow vector V_n, defined as $V_n = v_n e^{in\Psi_n}$, and can be calculated according to

$$v_n = \langle \cos[n(\varphi - \Psi_n)] \rangle, \tag{2}$$

where the brackets denote an average over all particles in all events. Since the symmetry planes are not accessible experimentally, the flow coefficients are estimated solely from the azimuthal angles of the particles emitted in the transverse plane. Measurements of different anisotropic flow coefficients at both RHIC [14–30] and the LHC [31–45] have not only confirmed the production of a strongly coupled quark gluon plasma (sQGP) but have also contributed in constraining the value of its shear viscosity over entropy density (η/s) which is very close to the lower limit of $1/4\pi$ conjectured by AdS/CFT [46]. In addition, the comparison between experimental data [40] and viscous hydrodynamical calculations [47] showed that higher order flow coefficients and more importantly their transverse momentum dependence are more sensitive probes than lower order coefficients, i.e. v_2 and v_3, to the initial spatial irregularity and its fluctuations [10].
This initial state spatial irregularity is usually quantified with the standard (moment-defined) anisotropy coefficients, ε_n. In the Monte-Carlo Glauber model, ε_n and its corresponding initial symmetry plane, Φ_n can be calculated from the transverse positions of the nucleons participating in a collision according to [9, 48]

$$\varepsilon_n e^{in\Phi_n} = \frac{\langle r^n e^{in\phi} \rangle}{\langle r^n \rangle} (\text{for } \mathrm{n} > 1), \tag{3}$$

where the brackets denote an average over the transverse position of all participating nucleons that have an azimuthal angle ϕ and a polar distance from the centre r. Model calculations show that v_2 and to a large extent, v_3 are for a wide range of impact parameters linearly proportional to their corresponding initial spatial anisotropy coefficients, ε_2 and ε_3, respectively [9] while for larger values of n, v_n scales with a cumulant-based definition of initial anisotropic coefficients. As an example, the fourth order

spatial anisotropy is given by

$$\varepsilon_4' e^{i4\Phi_4'} = \varepsilon_4 e^{i4\Phi_4} + \frac{3\langle r^2 \rangle^2}{\langle r^4 \rangle} \varepsilon_2^2 e^{i4\Phi_2},$$ (4)

where ε_4' is the cumulant-based spatial anisotropy coefficient [49, 50], and the second term in the right hand side of Eq. 4 reveals a non-linear dependence of ε_4' on the lower order ε_2. This further supports the earlier ideas that the higher order flow coefficients, V_n ($n > 3$) obtain contributions not only from the linear response of the system to ε_n, but also a non-linear response proportional to the product of lower order initial spatial anisotropies [51, 52].

In particular, for a single event, V_n with $n = 4, 5, 6$ can be decomposed to the linear (V_n^{L}) and non-linear (V_n^{NL}) modes according to

$$\begin{aligned}
V_4 &= V_4^{\mathrm{L}} + V_4^{\mathrm{NL}} = V_4^{\mathrm{L}} + \chi_{4,22}(V_2)^2, \\
V_5 &= V_5^{\mathrm{L}} + V_5^{\mathrm{NL}} = V_5^{\mathrm{L}} + \chi_{5,32}V_3 V_2, \\
V_6 &= V_6^{\mathrm{L}} + V_6^{\mathrm{NL}} = V_6^{\mathrm{L}} + \chi_{6,222}(V_2)^3 + \chi_{6,33}(V_3)^2 + \chi_{6,42}V_2 V_4^{\mathrm{L}},
\end{aligned}$$ (5)

where $\chi_{n,mk}$, known as non-linear flow mode coefficients, quantify the contributions of the non-linear modes to the total V_n [52, 53]. For simplicity the magnitude of the total V_n will be referred to as anisotropic flow coefficient (v_n) in the rest of this article. The magnitude of the p_{T}-differential non-linear modes for higher order flow coefficients, v_n^{NL}, can be written as:

$$v_{4,22}(p_{\mathrm{T}}) = \frac{\langle v_4(p_{\mathrm{T}}) v_2^2 \cos(4\Psi_4 - 4\Psi_2) \rangle}{\sqrt{\langle v_2^4 \rangle}} \approx \langle v_4(p_{\mathrm{T}}) \cos(4\Psi_4 - 4\Psi_2) \rangle,$$ (6)

$$v_{5,32}(p_{\mathrm{T}}) = \frac{\langle v_5(p_{\mathrm{T}}) v_3 v_2 \cos(5\Psi_5 - 3\Psi_3 - 2\Psi_2) \rangle}{\sqrt{\langle v_3^2 v_2^2 \rangle}} \approx \langle v_5(p_{\mathrm{T}}) \cos(5\Psi_5 - 3\Psi_3 - 2\Psi_2) \rangle,$$ (7)

$$v_{6,33}(p_{\mathrm{T}}) = \frac{\langle v_6(p_{\mathrm{T}}) v_3^2 \cos(6\Psi_6 - 6\Psi_3) \rangle}{\sqrt{\langle v_3^4 \rangle}} \approx \langle v_6(p_{\mathrm{T}}) \cos(6\Psi_6 - 6\Psi_3) \rangle,$$ (8)

$$v_{6,222}(p_{\mathrm{T}}) = \frac{\langle v_6(p_{\mathrm{T}}) v_2^3 \cos(6\Psi_6 - 6\Psi_2) \rangle}{\sqrt{\langle v_2^6 \rangle}} \approx \langle v_6(p_{\mathrm{T}}) \cos(6\Psi_6 - 6\Psi_2) \rangle,$$ (9)

where brackets denote an average over all events. The approximation is valid assuming a weak correlation between the lower ($n = 2, 3$) and higher ($n > 3$) order flow coefficients [51, 54].

Various measurements of the p_{T}-differential anisotropic flow, $v_n(p_{\mathrm{T}})$, of charged particles [32, 37, 42, 44, 45, 55] have provided a testing ground for model calculations that attempt to describe the dynamical evolution of the system created in heavy-ion collisions. Early predictions showed that the p_{T}-differential anisotropic flow for different particle species can reveal more information about the equation of state, the role of the highly dissipative hadronic rescattering phase as well as probing particle production mechanisms [56, 57]. In order to test these predictions, $v_n(p_{\mathrm{T}})$ have been measured for different particle species at RHIC [14–17] and at the LHC [38, 39, 41, 43]. These measurements reveal a characteristic mass dependence of $v_n(p_{\mathrm{T}})$ in the low transverse momentum region ($p_{\mathrm{T}} < 3$ GeV/c), a result of an interplay between radial and anisotropic flow, and mass dependent thermal velocities [56, 57]. In the intermediate p_{T} region ($p_{\mathrm{T}} \sim 3$ GeV/c) the measurements indicate a particle type grouping where baryons have a

larger v_n than the one of mesons. This feature was explained in a dynamical model where flow develops at the partonic level followed by quark coalescence into hadrons [58, 59]. In this picture the invariant spectrum of produced particles is proportional to the product of the spectra of their constituents and, in turn, the flow coefficient of produced particles is the sum of the v_n values of their constituents. This leads to the so-called number of constituent quarks (NCQ) scaling, observed to hold at an approximate level of $\pm 20\%$ for $p_{\mathrm{T}} > 3$ GeV/c [17, 38, 39, 60].

The measurements of non-linear flow modes in different collision centralities could pose a challenge to hydrodynamic models and have the potential to further constrain both the initial conditions of the collision system and its transport properties, i.e. η/s and ζ/s [53, 61]. The p_{T}-dependent non-linear flow modes of identified particles, in particular, allow to test the effect of late-stage interactions in the hadronic rescattering phase, as well as the effect of particle production via the coalescence mechanism to the development of the mass ordering at low p_{T} and particle type grouping in the intermediate p_{T} region, respectively [32, 41].

In this article, we report the first results of the p_{T}-differential non-linear flow modes, i.e. $v_{4,22}$, $v_{5,32}$, $v_{6,33}$ and $v_{6,222}$ for $\pi^{\pm}$, $\mathrm{K}^{\pm}$, $\mathrm{K}^0_{\mathrm{S}}$, $\mathrm{p}+\overline{\mathrm{p}}$, $\Lambda+\overline{\Lambda}$ and φ measured in Pb–Pb collisions at a centre of mass energy per nucleon pair $\sqrt{s_{\mathrm{NN}}} = 5.02$ TeV, recorded by the ALICE experiment [62] at the LHC. The detectors and the selection criteria used in this analysis are described in Sec. 2 and 3, respectively. The analysis methodology and technique are presented in Sec. 4. In this article, the identified hadron under study and the charged reference particles are obtained from different, non-overlapping pseudorapidity regions. The azimuthal correlations not related to the common symmetry plane (known as non-flow), including the effects arising from jets, resonance decays and quantum statistics correlations, are suppressed by using multi-particle correlations as explained in Sec. 4 and the residual effect has been taken into account in the systematic uncertainty, described in Sec. 5. All coefficients for charged particles were measured separately for particles and anti-particles and were found to be compatible within statistical uncertainties. The measurements reported in Sec. 6 are therefore an average of the results for both charges. The results are reported within the pseudorapidity range $|\eta| < 0.8$ at different collision centralities between 0–60% range of Pb–Pb collisions.

2 Experimental setup

ALICE [62, 63] is one of the four large experiments at the LHC, particularly designed to cope with the large charged-particle densities present in central Pb–Pb collisions [64]. By convention, the z-axis is parallel to the beam direction, the x-axis is horizontal and points towards the centre of the LHC, and the y-axis is vertical and points upwards. The apparatus consists of a set of detectors located in the central barrel, positioned inside a solenoidal magnet which generates a 0.5 T field parallel to the beam direction, and a set of forward detectors.

The Inner Tracking System (ITS) [62] and the Time Projection Chamber TPC [65] are the main tracking detectors of the central barrel. The ITS consists of six layers of silicon detectors employing three different technologies. The two innermost layers, positioned at $r = 3.9$ cm and 7.6 cm, are Silicon Pixel Detectors (SPD), followed by two layers of Silicon Drift Detectors (SDD) ($r = 15$ cm and 23.9 cm). Finally, the two outermost layers are double-sided Silicon Strip Detectors (SSD) at $r = 38$ cm and 43 cm. The TPC has a cylindrical shape with an inner radius of about 85 cm, an outer radius of about 250 cm, and a length of 500 cm and it is positioned around the ITS. It provides full azimuthal coverage in the pseudorapidity range $|\eta| < 0.9$.

Charged particles were identified using the information from the TPC and the TOF detectors [62]. The TPC allows for a simultaneous measurement of the momentum of a particle and its specific energy loss $\langle \mathrm{d}E/\mathrm{d}x \rangle$ in the gas. The detector provides a separation more than 2 standard deviations for different hadron species at $p_{\mathrm{T}} < 0.7$ GeV/c and the possibility to identify particles on a statistical basis in the

relativistic rise region of dE/dx (i.e. $2 < p_{\mathrm{T}} < 20$ GeV/c) [63]. The dE/dx resolution for the 5% most central Pb–Pb collisions is 6.5% and improves for more peripheral collisions. The TOF detector is situated at a radial distance of 3.7 m from the beam axis, around the TPC and provides a 3σ separation between π–K and K–p up to $p_{\mathrm{T}} = 2.5$ GeV/c and $p_{\mathrm{T}} = 4$ GeV/c, respectively [63]. This is done by measuring the flight time of particles from the collision point with a resolution of about 80 ps. The start time for the TOF measurement is provided by the T0 detectors, two arrays of Cherenkov counters positioned at opposite sides of the interaction points covering $4.6 < \eta < 4.9$ (T0A) and $-3.3 < \eta < -3.0$ (T0C). The start time is also determined using a combinatorial algorithm that compares the timestamps of particle hits measured by the TOF to the expected times of the tracks, assuming a common event time t_{ev} [63]. Both methods of estimating the start time are fully efficient for Pb–Pb collisions up to 80% centrality interval.

A set of forward detectors, the V0 scintillator arrays [66], were used in the trigger logic and for the determination of the collision centrality. The V0 consists of two detectors, the V0A and the V0C, positioned on each side of the interaction point, covering the pseudorapidity ranges of $2.8 < \eta < 5.1$ and $-3.7 < \eta < -1.7$, respectively.

For more details on the ALICE apparatus and the performance of the detectors, see Refs. [62, 63].

3   Event sample, track selection and particle identification

3.1   Trigger selection and data sample

The analysis is performed on minimum bias Pb–Pb collision data at $\sqrt{s_{\mathrm{NN}}} = 5.02$ TeV collected by ALICE in 2015. These events were triggered by the coincidence between signals from both V0A and V0C detectors. An offline event selection, exploiting the signal arrival time in V0A and V0C, measured with a 1 ns resolution, was used to discriminate beam induced-background (e.g. beam gas events) from collision events. This led to a reduction of background events in the analysed samples to a negligible fraction ($< 0.1\%$) [63]. Events with multiple reconstructed vertices were rejected by comparing multiplicity estimates from the V0 detector to tracking detectors at mid-rapidity, exploiting the difference in readout times between the systems. The fraction of pileup events left after applying the dedicated pileup removal criteria is negligible. All events selected for the analysis had a reconstructed primary vertex position along the beam axis (z_{vtx}) within 10 cm from the nominal interaction point. After all the selection criteria, a filtered data sample of approximately 40 million Pb–Pb events in 0-60% centrality interval was analysed to produce the results presented in this article.

Events were classified according to fractions of the inelastic hadronic cross-section. The 0-5% interval represents the most central interactions (i.e. smallest impact parameter) and is referred to as most central collisions. On the other hand, the 50-60% centrality interval corresponds to the most peripheral (i.e. largest impact parameter) collisions in the analysed sample. The centrality of the collision was estimated using the signal magnitude measured in the V0 detectors which is related to the number of particles crossing their sensitive areas. Details about the centrality determination can be found in Ref. [67].

3.2   Selection of primary $\pi^{\pm}$, $\mathrm{K}^{\pm}$ and $\mathrm{p} + \overline{\mathrm{p}}$

In this analysis, tracks are reconstructed using the information from the TPC and the ITS detectors. The tracking algorithm, based on the Kalman filter [68, 69], starts from a collection of space points (referred to as clusters) inside the TPC, and provides the quality of the fit by calculating its χ^2 value. Each space point is reconstructed at one of the TPC padrows, where the deposited ionisation energy is also measured. The specific ionisation energy loss $\langle \mathrm{dE/dx} \rangle$ is estimated using a truncated mean, excluding the 40% highest-charge clusters associated to the track. The obtained $\langle \mathrm{dE/dx} \rangle$ has a resolution, which we later refer to as σ_{TPC}. The tracks are propagated to the outer layer of the ITS, and the tracking algorithm attempts to identify space points in each one of the consecutive layers, reaching the innermost ones (i.e. SPD). The track parameters are then updated using the combined information from both the TPC and the ITS detectors.

Primary charged pions, kaons and (anti-)protons were required to have at least 70 reconstructed space points out of the maximum of 159 in the TPC. The average of the track fit per TPC space point per degree of freedom (see [63] for details) was required to be below 4. These selections reduce the contribution from short tracks, which are unlikely to originate from the primary vertex. To reduce the contamination by secondary tracks from weak decays or from the interaction with the material, only particles within a maximum distance of closest approach (DCA) between the tracks and the primary vertex in both the transverse plane ($\mathrm{DCA}_{xy} < 0.0105 + 0.0350(p_{\mathrm{T}} c/\mathrm{GeV})^{-1.1}$ cm) and the longitudinal direction ($\mathrm{DCA}_{\mathrm{z}} < 2$ cm) were analysed. Moreover, the tracks were required to have at least two associated ITS clusters in addition to having a hit in either of the two SPD layers. This selection leads to an efficiency of about 80% for primary tracks at $p_{\mathrm{T}} \sim 0.6$ GeV/c and a contamination from secondaries of about 5% at $p_{\mathrm{T}} = 1$ GeV/c [70]. These values depend on particle species and transverse momentum [70].

The particle identification (PID) for pions ($\pi^{\pm}$), kaons ($\mathrm{K}^{\pm}$) and protons ($\mathrm{p} + \overline{\mathrm{p}}$) used in this analysis relies on the two-dimensional correlation between the number of standard deviations in units of the resolution from the expected signals of the TPC and the TOF detectors similar to what was reported in [38, 39, 41]. In this approach particles were selected by requiring their standard deviations from the

209 $\langle dE/dx \rangle$ and t_{TOF} values to be less than a p_{T}-dependent value, maintaining a minimum purity of 90% for
210 $\pi^{\pm}$ and 75% for $K^{\pm}$ and 80% for $p + \overline{p}$. In order to further reduce the contamination from other species,
211 the standard deviation of a given track was required to be the minimum among other candidate species.

212 In addition, for the systematics (see section 5) the minimum purity was varied to more strict values, a con-
213 dition that becomes essential with increasing transverse momentum where the relevant detector response
214 for different particle species starts to overlap. The results for all three particle species were extrapolated
215 to 100% purity and the uncertainty from the extrapolation was also considered in the estimation of the
216 total systematic uncertainty.

3.3 Reconstruction of K_S^0, $\Lambda + \overline{\Lambda}$ and ϕ meson

218 In this analysis, the K_S^0 and $\Lambda + \overline{\Lambda}$ are reconstructed via the following fully hadronic decay channels:
219 $K_S^0 \rightarrow \pi^+ + \pi^-$ and $\Lambda(\overline{\Lambda}) \rightarrow p(\bar{p}) + \pi^-(\pi^+)$ with branching ratios of 69.2% and 63.9% [71], respectively.
220 The reconstruction is performed by identifying the candidates of secondary vertices, denoted as V^0s,
221 from which two oppositely-charged decay products originate. Such candidates are obtained during data
222 processing by looking for characteristic V-shaped decay topology among pairs of reconstructed tracks.

223 The daughter tracks were reconstructed within $|\eta| < 0.8$, while the criteria on the number of TPC space
224 points, the number of crossed TPC padrows, and the percentage of the expected TPC space points used
225 to reconstruct a track are identical to those applied for primary particles. In addition, the minimum DCA
226 of daughter tracks to the primary vertex is 0.1 cm. Furthermore, the maximum DCA of daughter tracks
227 to the secondary vertex is 0.5 cm to ensure that they are products of the same decay. To suppress the
228 combinatorial background, PID is applied for the daughter particles in the whole p_{T} region by requiring
229 the particle to be within $3\sigma_{\text{TPC}}$ for a given species hypothesis.

230 To reject secondary vertices arising from decays into more than two particles, the cosine of the pointing
231 angle, θ_p, is required to be larger than 0.998. This angle is defined as the angle between the momentum
232 vector of the V^0 candidate assessed at its decay vertex and the line connecting the V^0 decay vertex to
233 the primary vertex and has to be close to 1 as a result of momentum conservation. In addition, only
234 the candidates reconstructed between 5 and 100 cm from the nominal primary vertex in radial direction
235 are accepted. The lower value is chosen to avoid any bias from the efficiency loss when secondary
236 tracks are being wrongly matched to clusters in the first layer of the ITS, where the occupancy is the
237 largest. To assess the systematic uncertainty related to the contamination from $\Lambda + \overline{\Lambda}$ and electron-
238 positron pairs coming from γ-conversions to the K_S^0 sample, a selection in the Armenteros-Podolanski
239 variables [72] is applied for the K_S^0 candidates, rejecting ones with $q \leq 0.2|\alpha|$. Here q is the momentum
240 projection of the positively charged daughter track in the plane perpendicular to the V^0 momentum and
241 $\alpha = (p_L^+ - p_L^-)/(p_L^+ + p_L^-)$ with $p_L^{\pm}$ the projection of the positive or negative daughter tracks' momentum
242 onto the momentum of the V^0.

243 The reconstruction of ϕ meson candidates is done via the hadronic decay channel: $\varphi \rightarrow K^+ + K^-$ with
244 a branching ratio of 48.9% [71]. The ϕ meson candidates were reconstructed from the charged tracks
245 passing all criteria for charged kaons. These kaon daughters are identified by utilising the Bayesian PID
246 approach [73] with a minimum probability threshold of 85% using the TPC and TOF detectors. Addi-
247 tionally, to reduce combinatorial background, a track is identified as kaon if it has the highest probability
248 among all considered species (e, μ, $\pi^{\pm}$, $K^{\pm}$ and $p + \overline{p}$). The vector sum of all possible pairs of charged
249 kaons are called ϕ candidates. The invariant mass distribution ($M_{\text{inv}}^{K^+K^-}$) of ϕ candidates is then obtained
250 in various p_{T} intervals by subtracting a combinatorial background yield from the candidate yield. This
251 combinatorial background yield is estimated from like-sign kaon pairs (unphysical ϕ state with total
252 charge of ± 2) normalised to the candidate yield.

4 Analysis method

In this article the p_{T}-differential non-linear flow modes are calculated according to Eqs. 12-15. Each event is divided into two subevents "A" and "B", covering the ranges $-0.8 < \eta < 0.0$ and $0.0 < \eta < 0.8$, respectively. Thus $v_{n,mk}(p_{\mathrm{T}})$ is a weighted average of $v_{n,mk}^{\mathrm{A}}(p_{\mathrm{T}})$ and $v_{n,mk}^{\mathrm{B}}(p_{\mathrm{T}})$. The measured $v_{n,mk}^{\mathrm{A(B)}}(p_{\mathrm{T}})$ coefficients are calculated using $d_{n,mk}(p_{\mathrm{T}})$ and $c_{mk,mk}$ multi-particle correlators given by

$$d_{n,mk}(p_{\mathrm{T}}) = \langle v_n(p_{\mathrm{T}})v_m v_k \cos(n\Psi_n - m\Psi_m - k\Psi_k)\rangle, \tag{10}$$

$$c_{mk,mk} = \langle v_m^2 v_k^2 \rangle. \tag{11}$$

These correlators are obtained using the Generic Framework with sub-event method originally used in [53], which allows precise non-uniform acceptance and efficiency corrections. In this analysis, $d_{n,mk}(p_{\mathrm{T}})$ is measured by correlating the azimuthal angle of particle of interest ($\varphi_1(p_{\mathrm{T}})$) from subevent "A"("B") with that of reference particles from subevent "B"("A") and $c_{mk,mk}$ by selecting half of the reference particles from subevent "A" and the other half from "B". Thus, Eqs.6 to 9 for $v_{n,mk}^{\mathrm{A}}(p_{\mathrm{T}})$ translate to

$$v_{4,22}^{\mathrm{A}}(p_{\mathrm{T}}) = \frac{d_{4,22}^{\mathrm{A}}(p_{\mathrm{T}})}{\sqrt{c_{22,22}}} = \frac{\langle\langle\cos(4\varphi_1^A(p_{\mathrm{T}}) - 2\varphi_2^B - 2\varphi_3^B)\rangle\rangle}{\sqrt{\langle\langle\cos(2\varphi_1^A + 2\varphi_2^A - 2\varphi_3^B - 2\varphi_4^B)\rangle\rangle}}, \tag{12}$$

$$v_{5,32}^{\mathrm{A}}(p_{\mathrm{T}}) = \frac{d_{5,32}^{\mathrm{A}}(p_{\mathrm{T}})}{\sqrt{c_{32,32}}} = \frac{\langle\langle\cos(5\varphi_1^A(p_{\mathrm{T}}) - 3\varphi_3^B - 2\varphi_2^B)\rangle\rangle}{\sqrt{\langle\langle\cos(3\varphi_1^A + 2\varphi_2^A - 3\varphi_3^B - 2\varphi_4^B)\rangle\rangle}}, \tag{13}$$

$$v_{6,33}^{\mathrm{A}}(p_{\mathrm{T}}) = \frac{d_{6,33}^{\mathrm{A}}(p_{\mathrm{T}})}{\sqrt{c_{33,33}}} = \frac{\langle\langle\cos(6\varphi_1^A(p_{\mathrm{T}}) - 3\varphi_2^B - 3\varphi_3^B)\rangle\rangle}{\sqrt{\langle\langle\cos(3\varphi_1^A + 3\varphi_2^A - 3\varphi_3^B - 3\varphi_4^B)\rangle\rangle}}, \tag{14}$$

$$v_{6,222}^{\mathrm{A}}(p_{\mathrm{T}}) = \frac{d_{6,222}^{\mathrm{A}}(p_{\mathrm{T}})}{\sqrt{c_{222,222}}} = \frac{\langle\langle\cos(6\varphi_1^A(p_{\mathrm{T}}) - 2\varphi_2^B - 2\varphi_3^B - 2\varphi_4^B)\rangle\rangle}{\sqrt{\langle\langle\cos(2\varphi_1^A + 2\varphi_2^A + 2\varphi_3^A - 2\varphi_4^B - 2\varphi_5^B - 2\varphi_6^B)\rangle\rangle}}, \tag{15}$$

where $\langle\langle\rangle\rangle$ denotes an average over all particles and events.

This multi-particle correlation technique by construction removes a significant part of non-flow correlations. In order to further reduce residual non-flow contributions, a pseudorapidity gap was applied between the two pseudorapidity regions ($|\Delta\eta| > 0.4$). In addition, particles with like-sign charges were correlated. These two variations did not affect the results significantly but any variation was included in the final systematics in Tab. 1.

For charged hadrons, i.e. $\pi^{\pm}$, $K^{\pm}$ and $p + \overline{p}$, the $d_{n,mk}$ correlators are calculated on a track-by-track basis as a function of p_{T} for each centrality percentile. For particle species reconstructed on a statistical basis from decay products, i.e. K_S^0, $\Lambda + \overline{\Lambda}$ and ϕ meson, the selected sample contains both signal and the background. Therefore, the $d_{n,mk}$ correlators are measured as a function of invariant mass (M_{inv}) and p_{T} for each centrality percentile. The $d_{n,mk}$ vs. M_{inv} method is based on the additivity of correlations and is a weighted sum of the $d_{n,mk}^{\mathrm{sig}}$ and $d_{n,mk}^{\mathrm{bkg}}$ according to

$$d_{n,mk}^{\mathrm{total}}(M_{\mathrm{inv}}, p_{\mathrm{T}}) = \frac{N^{\mathrm{sig}}}{N^{\mathrm{sig}} + N^{\mathrm{bkg}}}(M_{\mathrm{inv}}, p_{\mathrm{T}}) d_{n,mk}^{\mathrm{sig}}(p_{\mathrm{T}}) + \frac{N^{\mathrm{bkg}}}{N^{\mathrm{sig}} + N^{\mathrm{bkg}}}(M_{\mathrm{inv}}, p_{\mathrm{T}}) d_{n,mk}^{\mathrm{bkg}}(M_{\mathrm{inv}}, p_{\mathrm{T}}), \tag{16}$$

where N^{sig} and N^{bkg} are signal and background yields obtained for each p_T interval and centrality percentile from fits to K^0_S, $\Lambda + \overline{\Lambda}$ and ϕ meson invariant mass distributions. To obtain the p_T-differential yield of K^0_S and $\Lambda + \overline{\Lambda}$, invariant mass distributions at various p_T intervals are parametrised as a sum of two Gaussian distribution and a third-order polynomial function. The latter is introduced to account for residual contamination (background yield) that are present in the K^0_S and $\Lambda + \overline{\Lambda}$ signals after the topological and daughter track selections. The K^0_S and $\Lambda + \overline{\Lambda}$ yields are extracted by integration of the Gaussian distribution. Similarly, to obtain the p_T-differential yield of ϕ-mesons, the invariant mass distributions of the candidate yield is parametrized as a sum of a Breit-Wigner distribution and a third-order polynomial function, the latter introduced to account for residual contamination.

To extract $d^{\text{sig}}_{n,mk}$ in a given p_T range, $d^{\text{total}}_{n,mk}(M_{\text{inv}})$ is fitted together with the fit values from the invariant mass distribution and parametrising $d^{\text{bkg}}_{n,mk}(M_{\text{inv}})$ with a first order polynomial function. Figure 1 illustrates this procedure for the ϕ-meson, with the invariant mass distribution in the upper panel and the measurement of $d^{\text{total}}_{4,22}(M_{\text{inv}})$ in the lower panel.
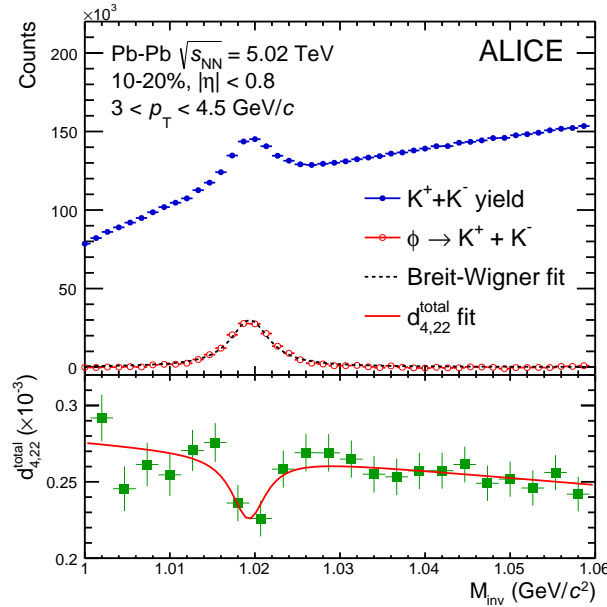

Figure 1: Reconstruction and $d_{4,22}$ measurement of ϕ-meson. Upper panel: extraction of N^{sig} and N^{bkg} by fitting the invariant mass (M_{inv}) distribution for ϕ-meson candidates from pair of kaons with opposite charges for $3 < p_T < 4.5$ GeV/c at 10-20% centrality interval, lower panel: extraction of $d^{sig}_{4,22}$ by fitting Eq. 16 to the invariant mass dependence of $d^{\text{total}}_{4,22}$.

5 Systematic uncertainties

The systematic uncertainties are estimated by varying the selection criteria for all particle species as well as the topological reconstruction requirements for K^0_S, $\Lambda + \overline{\Lambda}$ and ϕ. The contributions from different sources are extracted from the relative ratio of the p_T-differential $v_{n,mk}$ between the default selection criteria described in Section 3 and their variations summarised in this section. Sources with statistically significant contribution (where significance is evaluated as recommended in [74]) were added in quadrature to form the final value of the systematic uncertainties on the non-linear flow modes. An overview of the magnitude of the relative systematic uncertainties per particle species is given in Tab. 1 for $\pi^{\pm}$, $K^{\pm}$ and $p + \overline{p}$ and Tab. 2 for K^0_S, $\Lambda + \overline{\Lambda}$ and ϕ-meson. Systematic uncertainties are grouped into five categories, i.e. event selection, tracking, particle identification, topological cuts and non-flow contribution

298 and are described below.

299 The effects of event selection criteria on the measurements are studied by: (i) varying the primary vertex
300 position along the beam axis (z_{vtx}) from a nominal ± 10 cm to ± 8 cm and ± 6 cm; (ii) changing the
301 centrality estimator from the signal amplitudes in the V0 scintillator detectors to the number of clusters
302 in the first or second layer of SPD, (iii) analysing events recorded for different magnetic field polarities
303 independently; (iv) not rejecting all events with tracks caused by pileup.

304 Systematic uncertainties induced by the selection criteria imposed at the track level were investigated
305 by: (i) changing the tracking from global mode where combined track information from both TPC and
306 ITS detectors are used to what is referred to as hybrid mode in which track parameters from TPC are
307 used if the algorithm is unable to match the track reconstructed in the TPC with associated ITS clusters;
308 (ii) increasing the number of TPC space points from 60 up to 90 and (iii) decreasing the value of the χ^2
309 per TPC space point per degree of freedom from 4 to 3; (iv) varying the selection criteria on both the
310 transverse and longitudinal components of the DCA to estimate the impact of secondary particles from a
311 strict p_T-dependent cut to 0.15 cm and 2 cm to 0.2 cm, respectively.

312 Systematic uncertainties associated with the particle identification procedure were studied by varying the
313 PID method from a p_T-dependent one described in 3.2 to even stricter version where the purity increases
314 to higher than 95% ($\pi^{\pm}$), 80% ($K^{\pm}$) and 80% ($p + \bar{p}$) across the entire p_T range of study. The second
315 approach used relied on the Bayesian method with a probability of at least 80% which gives an increase
316 in purity to at least 97% ($\pi^{\pm}$), 87% ($K^{\pm}$) and 90% ($p + \bar{p}$) across the entire p_T range of study. To further
317 check the effect of contamination the purity of these species was extrapolated to 100%.

318 The topological cuts were also varied to account for the V^0 and ϕ-meson reconstruction. These selection
319 criteria are varied by (i) changing the reconstruction method for V^0 particles to an alternate technique
320 that uses raw tracking information during the Kalman filtering stage (referred to as online V0 finder); (ii)
321 varying the minimum radial distance from the primary vertex at which the V^0 can be produced from 5 cm
322 to 10 cm; (iii) changing the minimum value of cosine of pointing angle from 0.998 to 0.99; (iv) varying
323 the minimum number of TPC space points crossed by the V^0 daughter tracks from 70 to 90; (v) changing
324 the requirement on the minimum number of TPC space points that are used in the reconstruction of the
325 V^0 daughter tracks form 70 to 90; (vi) requesting a minimum ratio of crossed to findable TPC clusters
326 from 0.8 to 1.0; (vii) changing the minimum DCA of the V^0 daughter tracks to the primary vertex from
327 0.1 cm to 0.3 cm; (viii) changing the maximum DCA of the V^0 daughter tracks to the secondary vertex
328 from 0.5 cm to 0.3 cm; (ix) requiring a minimum p_T of the V^0 daughter tracks of 0.2 GeV/c.

329 In addition, the non-flow contribution is studied by (i) selecting like sign pairs of particles of interest and
330 reference particles to decrease the effect from decay of resonance particles; (ii) applying pseudorapidity
331 gaps between the two subevents from $|\Delta\eta| > 0.0$ to $|\Delta\eta| > 0.4$.

332 Tables 1 and 2 summarise the maximum relative systematic uncertainties for each individual systematic
333 source described above over all transverse momenta. The systematics are expressed for each non-linear
334 mode and particle species in a range to account for all centrality intervals in this article.

Error source	$v_{4,22}$			$v_{5,32}$			$v_{6,33}$			$v_{6,222}$		
	$\pi^\pm$	$K^\pm$	$p+\bar{p}$	$\pi^\pm$	$K^\pm$	$p+\bar{p}$	$\pi^\pm$	$K^\pm$	$p+\bar{p}$	$\pi^\pm$	$K^\pm$	$p+\bar{p}$
Primary z_{vtx}	0-2%	1-3%	0-3%	0-3%	1-3%	1-4%	3-5%	2-5%	3-5%	2-7%	2-7%	4-7%
Centrality estimator	0-4%	1-4%	1-5%	0-4%	1-3%	2-4%	4-10%	4-10%	5-10%	3-10%	5-10%	4-10%
Magnetic field polarity	0-2%	0-3%	0-3%	0-4%	0-5%	0-5%	0-10%	0-10%	0-10%	0-10%	0-10%	0-10%
Pileup rejection	0-4%	0-3%	0-4%	0-5%	1-5%	0-5%	5-7%	5-10%	5-8%	4-10%	4-10%	2-10%
Tracking mode	1-4%	1-5%	1-4%	2-6%	3-5%	2-8%	0-8%	0-7%	3-8%	1-10%	4-10%	2-10%
Number of TPC space-points	1-2%	0-2%	0-2%	0-3%	1-3%	1-3%	4-8%	3-8%	3-8%	2-8%	4-8%	4-8%
χ^2 per TPC space-point	0-2%	1-2%	1-3%	1-3%	1-3%	2-4%	3-5%	3-6%	3-6%	2-6%	4-7%	4-7%
DCAxy	0-2%	0-2%	1-3%	0-3%	1-3%	1-3%	2-7%	2-8%	4-8%	2-8%	4-8%	3-8%
DCAz	0-3%	0-2%	1-2%	1-2%	1-3%	2-3%	3-7%	3-7%	5-7%	2-7%	4-8%	2-8%
Particle identification	1-5%	1-5%	1-3%	1-5%	2-5%	1-5%	5-10%	5-10%	6-12%	4-12%	6-15%	4-15%
POI vs. RFP charges	0-2%	0-3%	2-3%	0-4%	0-4%	2-4%	0-4%	0-6%	0-6%	0%	0%	0%
η gap	1-3%	1-4%	1-2%	1-4%	1-4%	1-5%	0-5%	0-5%	0-5%	0%	0%	0%

Table 1: List of the maximum relative systematic uncertainties from each individual source for $v_{n,mk}$ of $\pi^\pm$, $K^\pm$ and $p+\bar{p}$. The uncertainties depend on the transverse momenta. Percentage ranges are given to account for all centrality intervals.

Error source	$v_{4,22}$			$v_{5,32}$		$v_{6,33}$	
	K_S^0	$\Lambda+\bar{\Lambda}$	ϕ	K_S^0	$\Lambda+\bar{\Lambda}$	K_S^0	$\Lambda+\bar{\Lambda}$
Primary z_{vtx}	0%	0-2%	1%	0%	0-3%	0%	1-3%
Tracking mode	-	-	2%	-	-	-	-
Number of TPC space-points	0-3%	1-2%	2%	0%	2%	0%	2%
Particle identification	-	-	4-6%	-	-	-	-
Reconstruction method (V^0 finder)	3-5%	2-3%	N/A	5%	1%	5%	1%
Decay radius	3-5%	1-3%	N/A	5-6%	0-2%	5%	2%
Ratio of crossed to findable TPC clusters	0-2%	0-3%	N/A	0%	1-2%	0%	3%
DCA decay products to primary vertex	2-5%	2-4%	N/A	4-5%	2-3%	5%	2-3%
DCA between decay products	0-3%	1-2%	N/A	0-4%	0-4%	0%	0-4%
Pointing angle $\cos(\theta_p)$	3-4%	0-2%	N/A	3-4%	0-3%	3%	1%
Minimum p_T of daughter tracks	1-3%	0-1%	N/A	2-3%	2-3%	0%	0-3%

Table 2: List of the maximum relative systematic uncertainties from each individual source for $v_{n,mk}$ of K_S^0, $\Lambda+\bar{\Lambda}$ and ϕ-meson. The uncertainties depend on the transverse momenta and centrality interval. Percentage ranges are given to account for all centrality intervals. "N/A" indicates that a certain check was not applicable to the given particle of interest. If a source was checked and proved to be of negligible effect, the field is marked with "-".

6 Results and discussion

In this section, the results of the p_T-dependent non-linear flow modes $v_{4,22}$, $v_{5,32}$, $v_{6,33}$ and $v_{6,222}$ of identified particles are presented for various centrality intervals in Pb–Pb collisions at $\sqrt{s_{NN}} = 5.02$ TeV. We first present the centrality and p_T dependence of $v_{n,mk}$ in Sec. 6.1. The scaling properties of non-linear flow modes are also discussed in this section. These results are compared with v_n measurements for the same particle species in Sec. 6.2. Finally, the comparison to two model calculations is shown in Sec. 6.3. Note that in some of the following sections the same data are used in different representations to highlight the various physics implications of the measurements in each section.

6.1 Centrality and p_T dependence of non-linear flow modes

Figure 2 presents the magnitude of the non-linear mode for the fourth order flow coefficient, $v_{4,22}(p_T)$, for $\pi^\pm$, $K^\pm$, K_S^0, $p+\bar{p}$, $\Lambda+\bar{\Lambda}$ and ϕ-meson in a wide range of centrality intervals, i.e. 0-5% up to 50-60%. For the ϕ-meson, the results are reported from 10-20% up to 40-50% centrality interval, where $v_{4,22}$ can be measured accurately. The magnitude of this non-linear flow mode rises steeply with increasing centrality interval from 0-5% to 40-50% for all particle species. This increase is expected as $v_{4,22}$ reflects the contribution of the second order eccentricity, ε_2, which increases from central to peripheral collisions, in v_4 [9, 53]. For more peripheral collisions (i.e. 50-60%) , the magnitude of $v_{4,22}$ is smaller than in the previous centrality intervals for all particle species. This effect that was observed also in v_n measure-

352 ments is probably due to the shorter lifetime of the produced system in more peripheral collisions, which
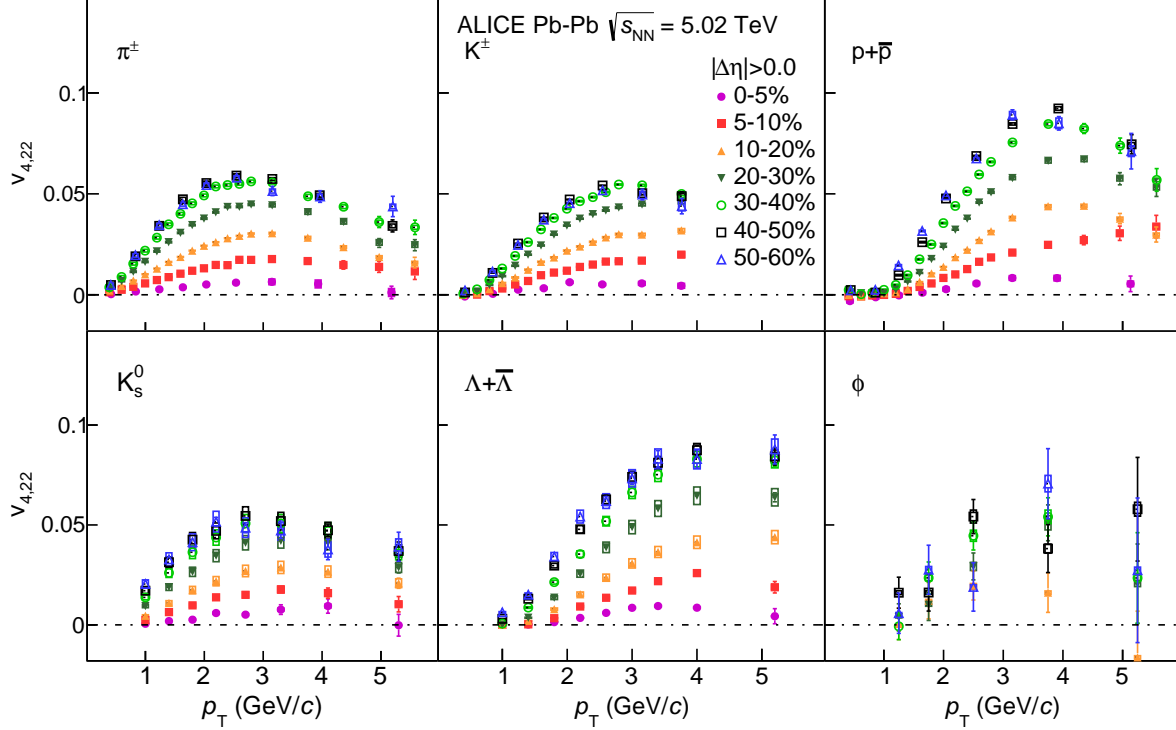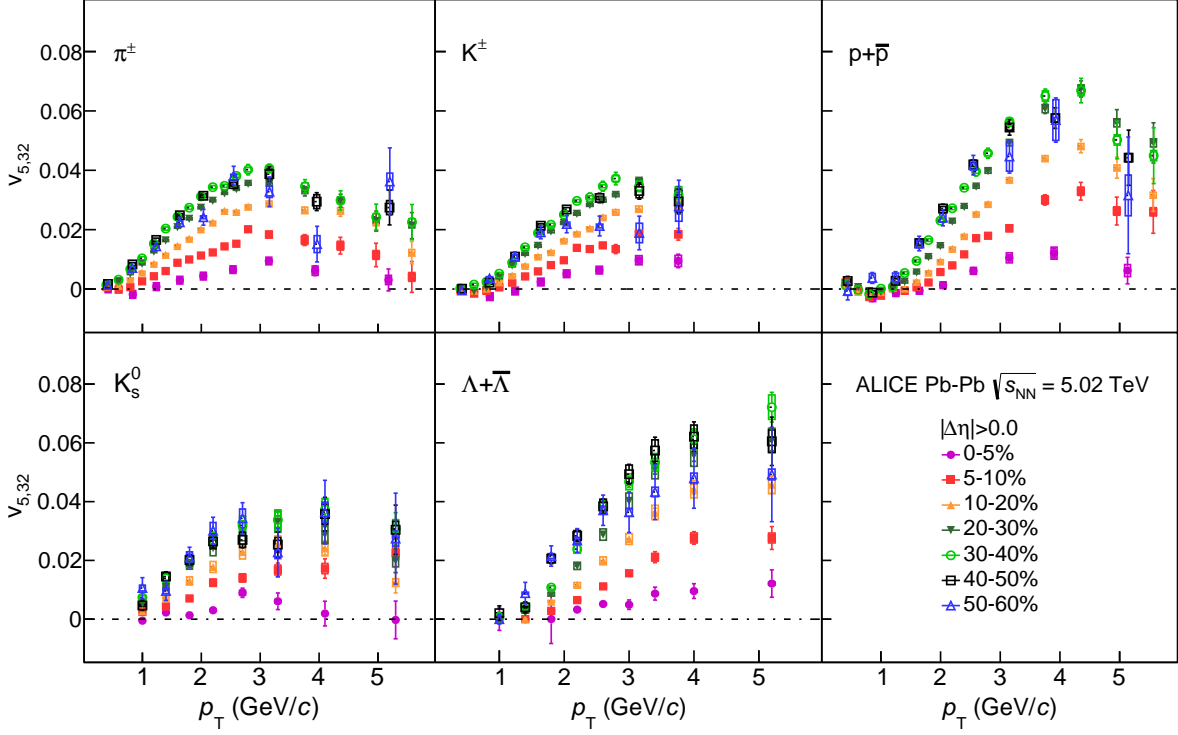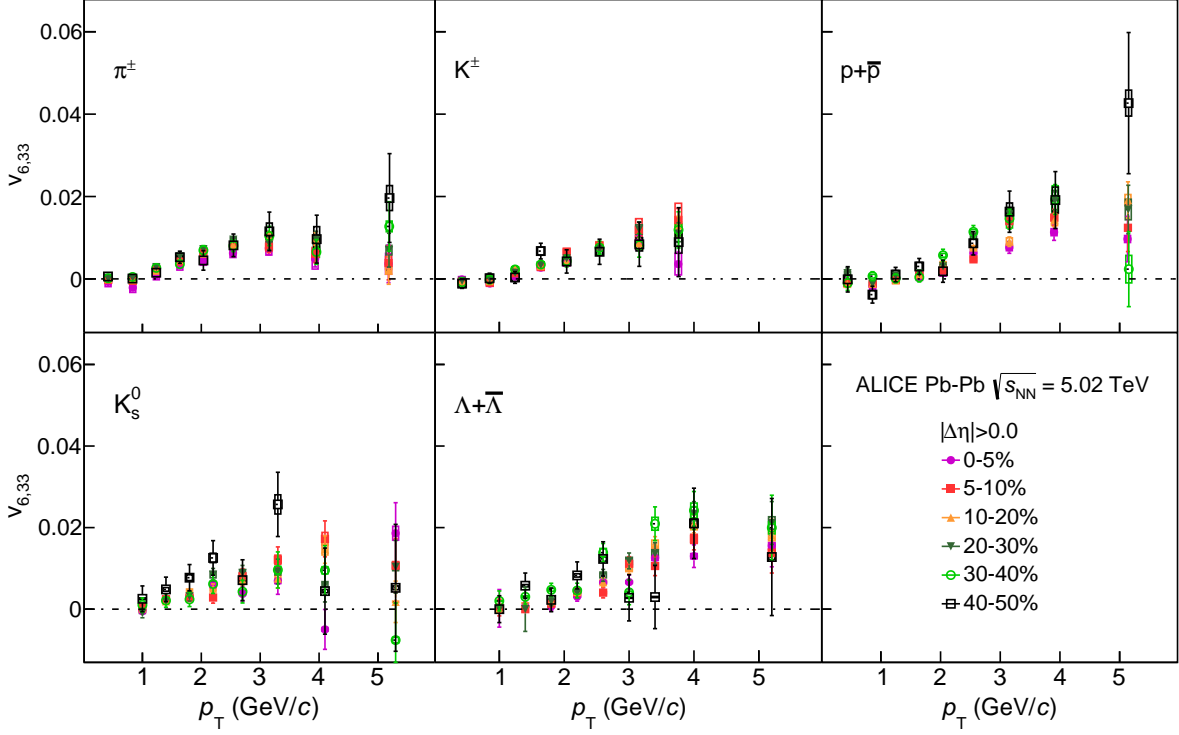353 prevents $v_{4,22}$ from developing further.

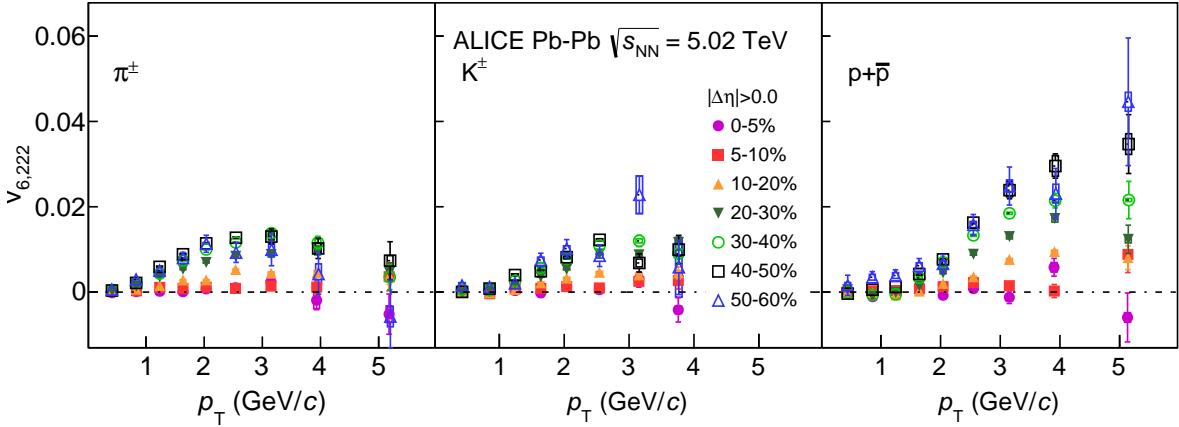**Figure 2:** The p_T-differential $v_{4,22}$ for different centrality intervals of Pb–Pb collisions at $\sqrt{s_{NN}} = 5.02$ TeV grouped by particle species. Statistical and systematic uncertainties are shown as bars and boxes, respectively.

354 Figure 3 presents the non-linear mode for the fifth order flow coefficient, i.e. $v_{5,32}(p_T)$, of $\pi^{\pm}$, $K^{\pm}$, K^0_S,
355 $p+\overline{p}$, and $\Lambda+\overline{\Lambda}$ for the same range of centrality intervals, i.e. 0-5% up to 50-60%. Statistical precision
356 limits extending the measurements of non-linear flow modes of ϕ-meson for $n > 4$. The measurements
357 show a significant increase in the magnitude of this non-linear flow mode with increasing centrality
358 percentile. This is due to the fact that $v_{5,32}(p_T)$ has a contribution from both ε_2 and ε_3. It is shown in
359 MC studies that ε_2 and to a smaller extent, ε_3 increase for peripheral collisions [9].

360 Figures 4 and 5 present the non-linear terms for the sixth order flow coefficient, i.e. $v_{6,33}(p_T)$ for $\pi^{\pm}$, $K^{\pm}$,
361 K^0_S, $p+\overline{p}$ and $\Lambda+\overline{\Lambda}$ at 0-5% up to 40-50% centrality intervals and $v_{6,222}(p_T)$ for $\pi^{\pm}$, $K^{\pm}$, $p+\overline{p}$ at 0-5% up
362 to 50-60% centrality intervals. As expected, measurements of $v_{6,222}(p_T)$ which probe the contribution of
363 ε_2, show an increase in the magnitude of this non-linear flow mode with increasing centrality percentile.
364 On the other hand, $v_{6,33}(p_T)$ measurements, which probe the contribution of ε_3, present little to no
365 dependence on centrality [53].

Figure 3: The p_T-differential $v_{5,32}$ for different centrality intervals of Pb–Pb collisions at $\sqrt{s_{NN}} = 5.02$ TeV grouped by particle species.

In Fig. 6 the same data points are grouped by centrality interval to highlight how $v_{4,22}$ develops for a given centrality for various particle species as a function of p_T. A clear mass ordering can be seen in the low p_T region (i.e. $p_T < 2.5$ GeV/c) for all collision centralities. This mass ordering arises from the interplay between radial flow and the initial spatial anisotropy, created from both the geometry and the fluctuating initial energy density profile. This creates a depletion in the particle spectra at lower p_T values which becomes larger in-plane than out-of plane due to the velocity profile. This naturally leads to lower $v_{4,22}(p_T)$ for heavier particles [56, 57, 75]. Similarly, Figs. 7, 8 and 9 show the p_T-differential $v_{5,32}$, $v_{6,33}$ and $v_{6,222}$ respectively, of different particle species for each centrality interval. A clear mass ordering is seen in the low p_T region, (i.e. $p_T < 2.5$ GeV/c), for $v_{5,32}(p_T)$, $v_{6,33}(p_T)$ and $v_{6,222}(p_T)$.

14

Figure 4: The p_T-differential $v_{6,33}$ for different centrality intervals of Pb–Pb collisions at $\sqrt{s_{NN}} = 5.02$ TeV grouped by particle species.

Figure 5: The p_T-differential $v_{6,222}$ for different centrality intervals of Pb–Pb collisions at $\sqrt{s_{NN}} = 5.02$ TeV grouped by particle species.

In addition, in the intermediate p_T region (for $p_T > 2.5$ GeV/c) the data points of Figs. 6-9 exhibit a particle type grouping. In particular, the data points form two groups, one for mesons and one for baryons with the values of $v_{n,mk}$ of the latter being larger. This particle type grouping was previously observed in v_n measurements of various particle species [14–17, 38, 39, 41]. This grouping was explained in Ref. [59]
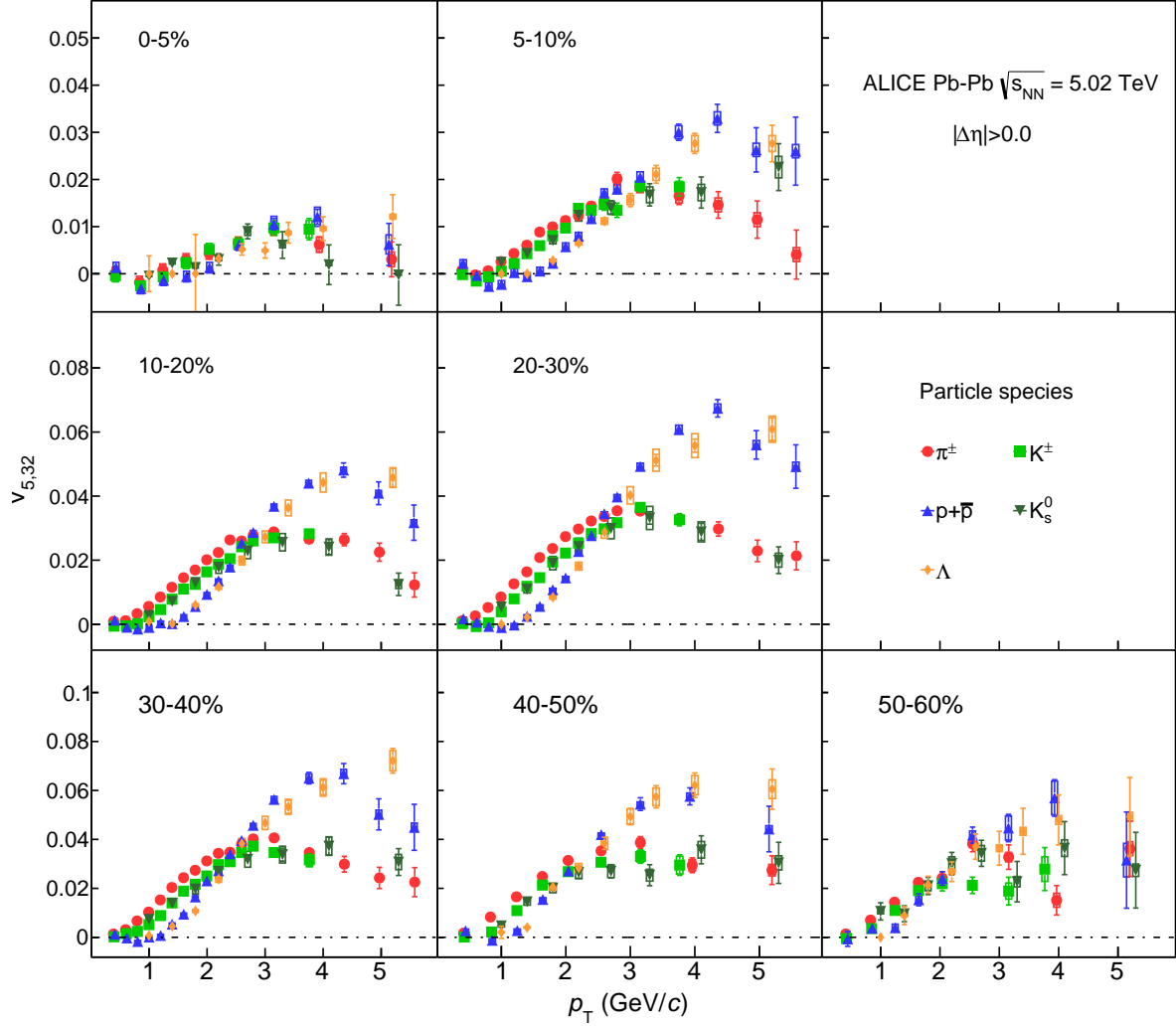
15
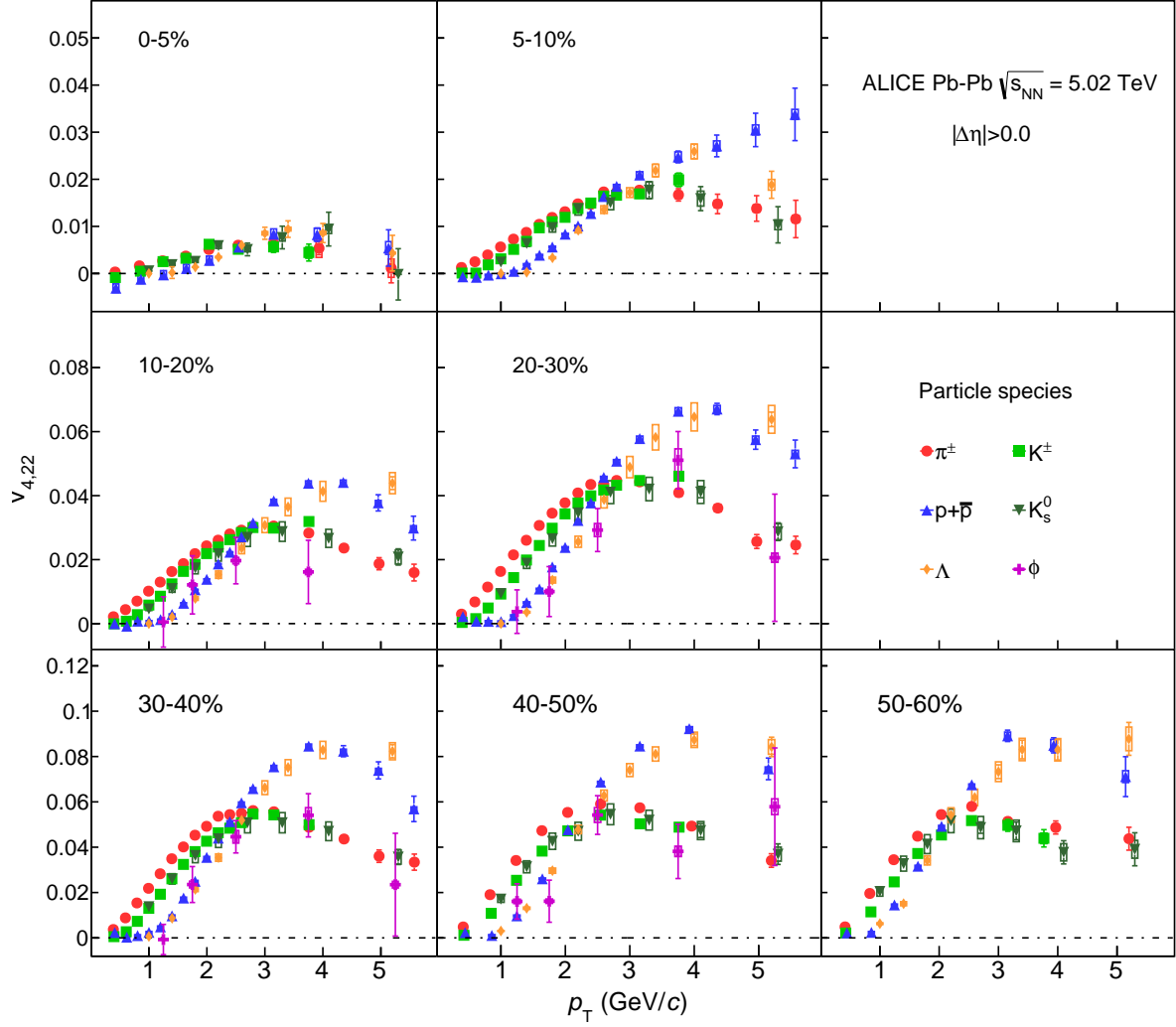
Figure 6: The p_T-differential $v_{4,22}$ for different particle species grouped into different centrality intervals of Pb–Pb collisions at $\sqrt{s_{NN}} = 5.02$ TeV.

in the picture of particle production via quark coalescence indicating that flow develops at the partonic stage. In this picture, known as NCQ scaling, the flow of mesons(baryons) are roughly twice(thrice) the flow of their constituent quarks in the intermediate transverse momentum region [58, 59]. ALICE measurements have shown that this scaling at the LHC energies holds at an approximate level of 20% for v_n [38, 39, 41].

Figures 10, 11, 12 and 13 present $v_{4,22}$, $v_{5,32}$, $v_{6,33}$ and $v_{6,222}$ respectively, scaled by the number of constituent quarks (n_q) as a function of p_T/n_q for $\pi^\pm$, $K^\pm$, K^0_S, $p+\bar{p}$, $\Lambda+\bar{\Lambda}$ and ϕ-meson grouped in different centrality intervals. The scaling is consistent with the observations reported for higher order anisotropic flow coefficients [41]. It is seen that for the non-linear flow modes this scaling holds at an approximate level ($\pm20\%$) for $p_T > 1$ GeV/c, where quark coalescence is expected to be the dominant process.
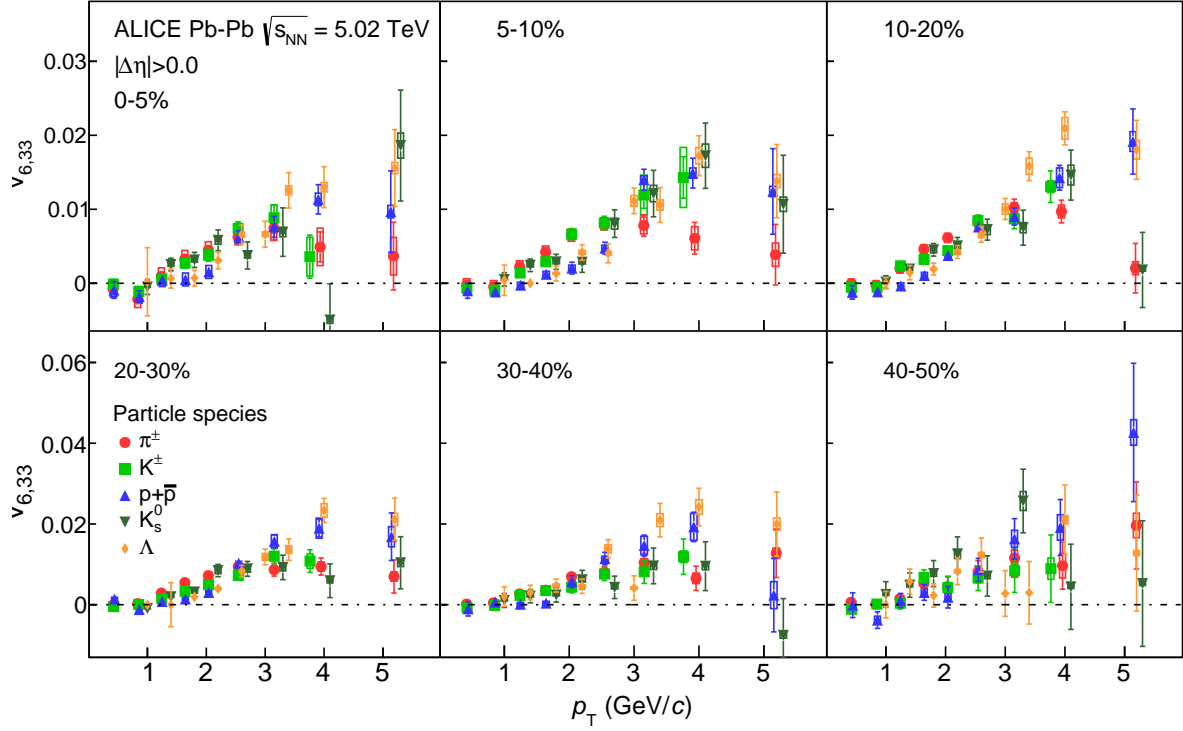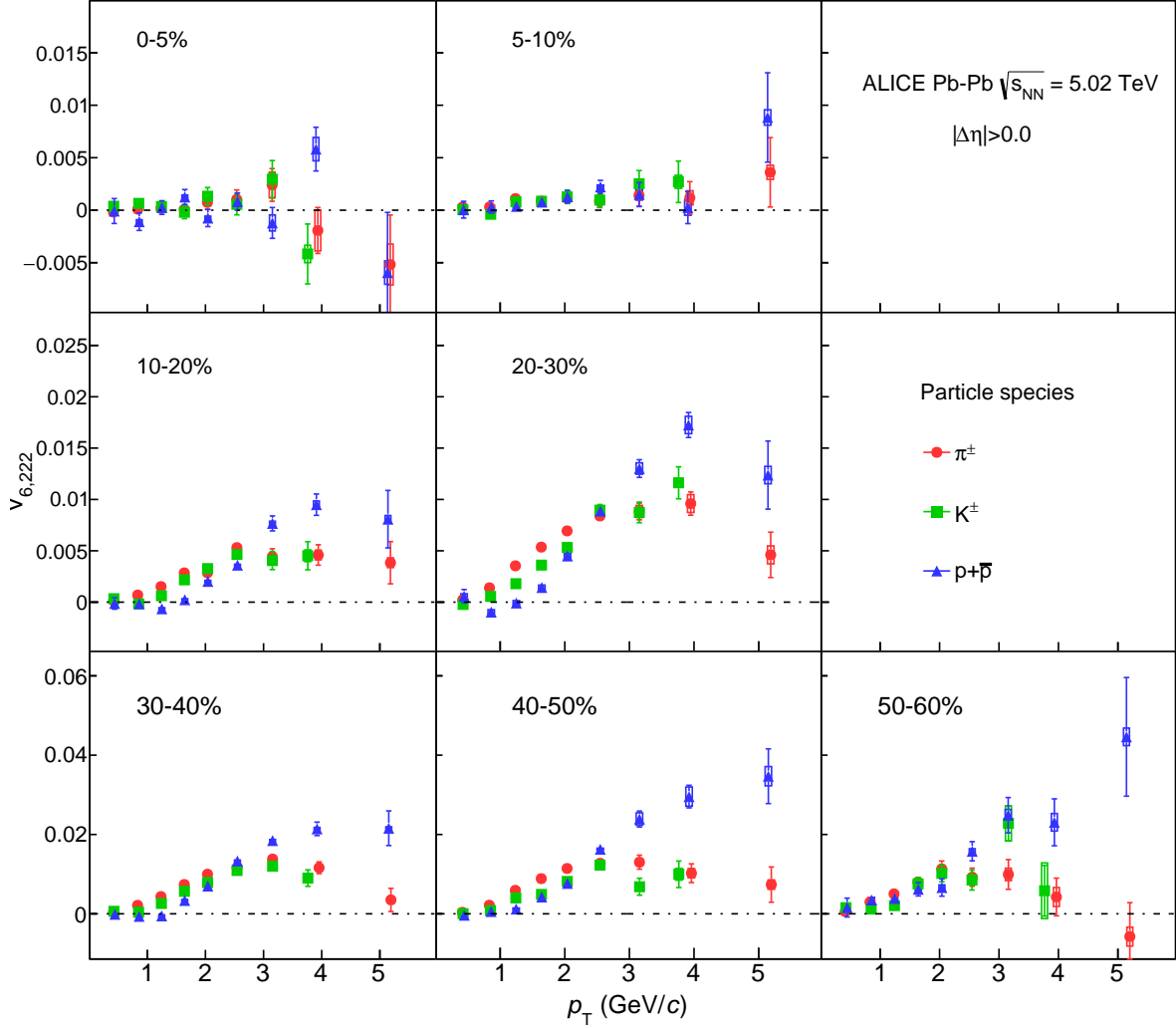
Figure 7: The p_T-differential $v_{5,32}$ for different particle species grouped into different centrality intervals of Pb–Pb collisions at $\sqrt{s_{NN}} = 5.02$ TeV.

6.2 Comparison with v_n of identified particles

The comparison of the features discussed before i.e. mass ordering and particle type grouping between the non-linear and the anisotropic flow coefficient is of particular interest. Based on a naive expectation the mass ordering should develop quantitatively in a different way between the non-linear (i.e. due to the dependence on ε_2^2) and the anisotropic flow coefficient. In parallel, if coalescence is the dominant particle production mechanism in the intermediate p_T region, one expects a similar grouping between v_n^{NL} and v_n. Such comparison could only be performed for $v_{4,22}(p_T)$ (this study) and $v_4(p_T)$ measurements [41] and was done by taking the difference between pions and protons at a given p_T in both modes and normalising it by the integrated flow of the corresponding mode for charged particles [40] ($[v_4^{\pi^\pm} - v_4^{p+\bar{p}}](p_T)/v_4^{h^\pm}$). This comparison is shown in Fig. 14 for 0-5% up to 40-50% centrality interval. It can be seen that in the low p_T region ($p_T < 2.5 - 3$ GeV/c) where the mass ordering is prominent, the data points exhibit a general agreement for all centrality intervals. However, there is a hint that the relative ratio for $v_{4,22}$ is smaller than the one of the v_4 for $p_T < 0.8$ GeV/c and for centrality ranges 0-30%. If this difference and its centrality dependence persists for lower values of p_T, it could indicate that the hydrodynamic evolution is reflected differently in v_4 and $v_{4,22}$ and could be explained by the contribution of ε_2^2. As it

17

Figure 8: The p_{T}-differential $v_{6,33}$ for different particle species grouped into different centrality intervals of Pb–Pb collisions at $\sqrt{s_{\mathrm{NN}}} = 5.02$ TeV.

was stated earlier, the mass splitting is a result of an interplay of radial and anisotropic flow, leading to a stronger in-plane expansion compared to out-of-plane, and the particle thermal motion. Particle of a larger mass have smaller thermal velocities, and are affected stronger by the difference between in- an out-of-plane expansion velocities, thus leading to the mass splitting of $v_n(p_{\mathrm{T}})$. The comparison of the p_{T} dependence of v_n^{NL} and v_n can provide a unique opportunity to test this picture, as it would allow to compare the results for the cases of exactly the same average radial flow and temperature, but differing by the anisotropic flow. On the other hand, in the intermediate p_{T} region ($p_{\mathrm{T}} > 2.5$ GeV/c), the same comparison shows that the results are compatible in all centrality intervals within one standard deviation. This implies a similar particle type grouping between v_4 and $v_{4,22}$ which is in line with the expectation that quark coalescence affects both flow modes similarly.
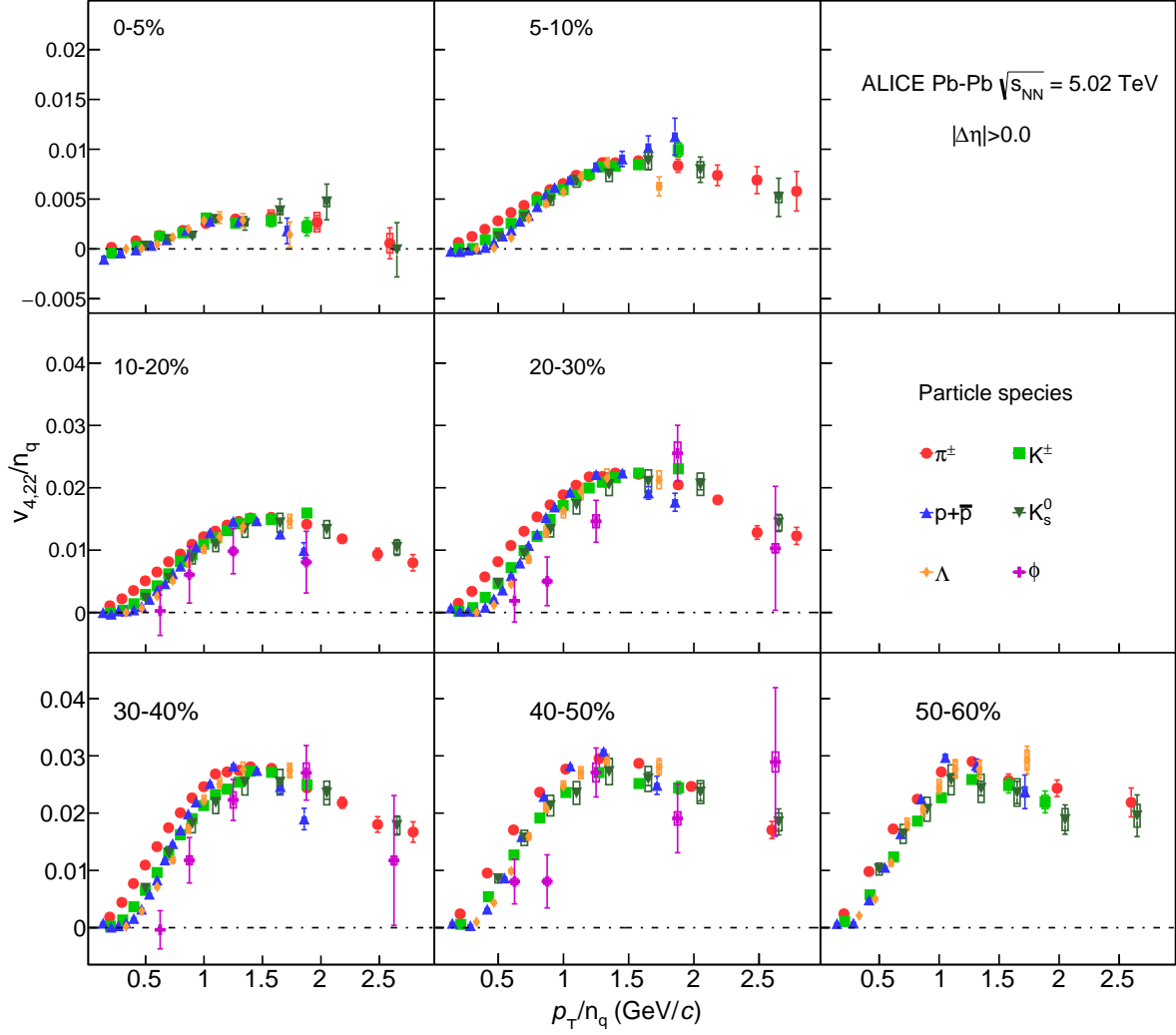
18

Figure 9: The p_T-differential $v_{6,222}$ for different particle species grouped into different centrality intervals of Pb–Pb collisions at $\sqrt{s_{NN}} = 5.02$ TeV.

6.3 Comparison with models

The comparison of various anisotropic flow measurements and hydrodynamic calculations have been presented and discussed in great details in [76–78]. A recent comparison between v_n measurements reported by ALICE [41] and two hydrodynamic calculations from [78] shed new light on the initial conditions and the transport properties of the created system in Pb–Pb collisions. Both hydrodynamic calculations are based on iEBE-VISHNU [79], an event-by-event version of the VISHNU hybrid model [80] coupling $2 + 1$ dimensional viscous hydrodynamics (VISH2+1) [81] to a hadronic cascade model (UrQMD). The initial conditions used for these calculations are described by AMPT [82] and TRENTo [83], both with τ_0=0.6 fm/c and T_{sw} =148 MeV [84]. For AMPT initial conditions, constant values of specific shear viscosity ($\eta/s = 0.08$, the lower limit conjectured by AdS/CFT) and bulk viscosity ($\zeta/s = 0$) are utilised. The version of the model that uses TRENTo [83] initial conditions incorporates a temperature dependent specific shear and bulk viscosity extracted from the global bayesian analysis
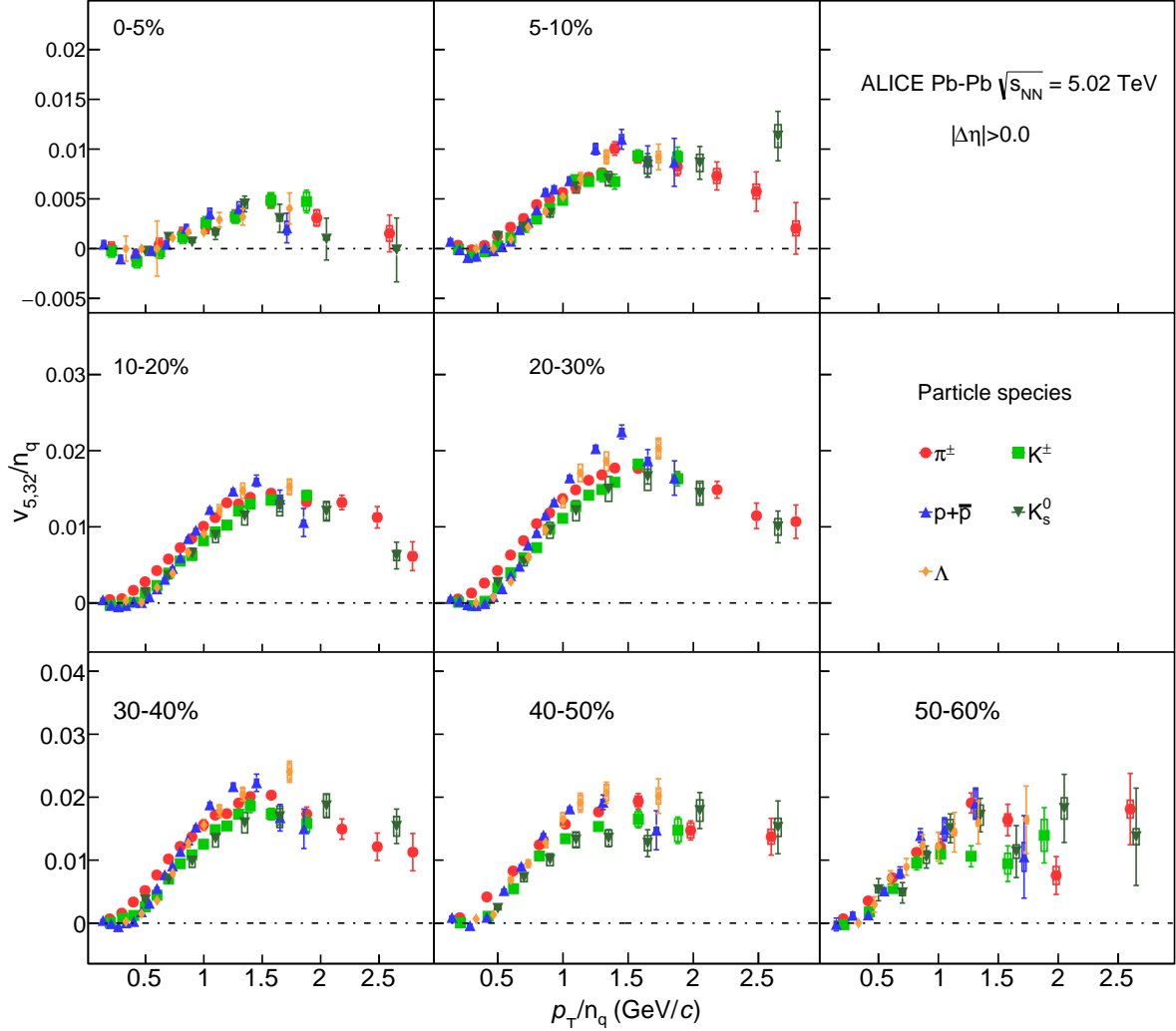
19

Figure 10: The p_T/n_q-dependence of $v_{4,22}/n_q$ for different particle species grouped into different centrality intervals of Pb–Pb collisions at $\sqrt{s_{NN}} = 5.02$ TeV.

[84]. [1]

The comparison between v_n measurements and these two hydrodynamic calculations illustrates a qualitative agreement. This agreement between the data and the models depends on the particle species, transverse momentum range and centrality percentile. Overall, the AMPT model reproduces these measurements more accurately than the TRENTo model [41]. In order to further investigate the performance of these two models in reproducing v_n measurements, the relative ratios between each model and the measurements of $\pi^{\pm}$, $K^{\pm}$ and $p + \bar{p}$ have been obtained. Table 3 summarises these relative ratios. The values represent the ranges across all centralities that each model is able to describe the measurements of v_n for each particle species. Comparison between the performance of the two models shows that the AMPT calculations reproduce v_2 slightly better that TRENTo. Both models reproduce the v_3 measurements relatively better than v_2, however AMPT performs better than TRENTo. Finally, the comparison between the models and v_4 measurements show that AMPT has an absolute better performance compared

---

[1]For simplicity in the rest of this article the model with AMPT initial conditions, $\eta/s = 0.08$ and $\zeta/s = 0$ is referred to as AMPT and the model with TRENTo initial conditions, $\eta/s(\text{T})$ and $\zeta/s(\text{T})$ is referred to as TRENTo.
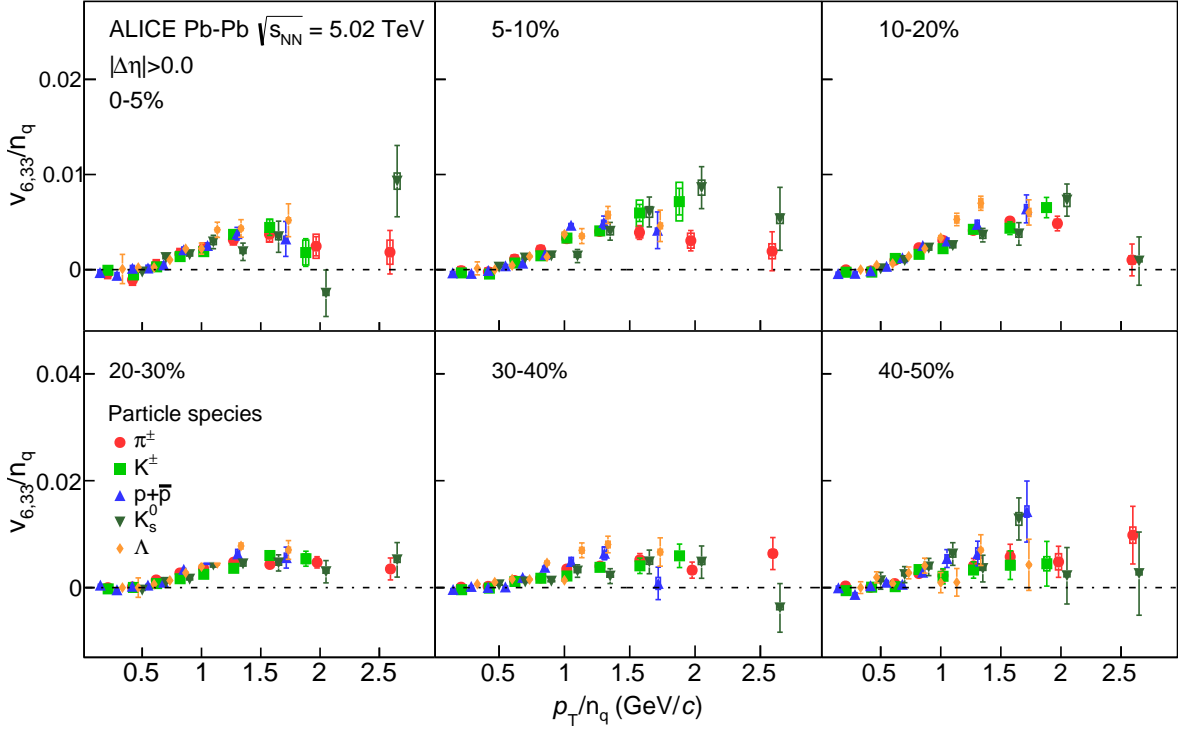
Figure 11: The p_T/n_q-dependence of $v_{5,32}/n_q$ for different particle species grouped into different centrality intervals of Pb–Pb collisions at $\sqrt{s_{NN}} = 5.02$ TeV.

to TRENTo. These values should be taken with caution as v_4 has larger uncertainties with respect to v_3 and v_2.

	v_2			v_3			v_4		
Error source	$\pi^{\pm}$	$K^{\pm}$	$p+\bar{p}$	$\pi^{\pm}$	$K^{\pm}$	$p+\bar{p}$	$\pi^{\pm}$	$K^{\pm}$	$p+\bar{p}$
AMPT calculations	3-13%	0-16%	0-20%	0-8%	5-12%	0-4%	6-12%	5-12%	0-4%
TRENTo calculations	6-17%	0-19%	3-19%	2-15%	7-22%	0-11%	7-25%	16-28%	0-21%

Table 3: List of minimum and maximum value of the fit to relative ratios between the data and each model for $v_n (n = 2, 3, 4)$ of $\pi^{\pm}$, $K^{\pm}$ and $p+\bar{p}$. The minimum and maximum are obtained from 0-5% up to 40-50% centrality intervals .

To achieve additional constraints on the initial conditions and transport properties of the system and test the validity of these hydrodynamic models, a comparison is performed between the measured p_T-dependent non-linear flow modes for $\pi^{\pm}$, $K^{\pm}$, $p+\bar{p}$, K_S^0 and $\Lambda+\overline{\Lambda}$ with the same two hydrodynamical calculations reported in [78]. Figures 15-18 present the comparison between the measurements and two model predictions for the p_T-differential $v_{4,22}$, $v_{5,32}$, $v_{6,33}$ and $v_{6,222}$, respectively, for $\pi^{\pm}$, $K^{\pm}$ and $p+\bar{p}$ and Figs. 19-21 present these comparisons for the p_T-differential $v_{4,22}$, $v_{5,32}$ and $v_{6,33}$ for K_S^0 and

Figure 12: The p_T/n_q-dependence of $v_{6,33}/n_q$ for different particle species grouped into different centrality intervals of Pb–Pb collisions at $\sqrt{s_{NN}} = 5.02$ TeV.

Error source	$v_{4,22}$			$v_{5,32}$			$v_{6,33}$			$v_{6,222}$		
	$\pi^\pm$	$K^\pm$	$p+\bar{p}$	$\pi^\pm$	$K^\pm$	$p+\bar{p}$	$\pi^\pm$	$K^\pm$	$p+\bar{p}$	$\pi^\pm$	$K^\pm$	$p+\bar{p}$
AMPT claculations	5-32%	2-30%	3-30%	3-28%	5-29%	1-65%	0-46%	0-46%	0-97%	6-52%	0-80%	0-118%
TRENTo calculations	0-30%	4-33%	0-21%	24-49%	33-97%	12-58%	0-43%	0-46%	0-95%	0-20%	0-34%	0-78%

Table 4: List of minimum and maximum value of the fit to relative ratios between the data and each model for $v_{n,mk}$ of $\pi^\pm$, $K^\pm$ and $p+\bar{p}$. The minimum and maximum are obtained from 0-10% up to 50-60% (40-50% for $v_{6,33}$) centrality intervals .

$\Lambda+\overline{\Lambda}$ at 0-10% up to 50-60% centrality interval (40-50% centrality interval for $v_{6,33}$) of Pb–Pb collisions at $\sqrt{s_{NN}} = 5.02$ TeV. The solid bands show the AMPT model and the hatched bands represent the TRENTo calculations. The bottom panels in each plot in Figs. 15-21 present the difference between the models and the measurement. Both TRENTo and AMPT models produce the mass ordering feature at $p_T < 2.5$ GeV/c for all non-linear flow modes. In particular, the comparison between the models and the measurements of $v_{4,22}$ reveals that TRENTo reproduces the data very well from 0-10% up to 30-40% centrality interval and fails to reproduce the measurements for the remaining more peripheral centrality intervals. On the other hand, AMPT overestimates the measurements from 0-10% up to 30-40% centrality interval. At 40-50% centrality interval, it reproduces the measurements for all particle species except $\pi^\pm$, where it slightly underestimates the results. For more peripheral collisions, it reproduces the $K^\pm$, $p+\bar{p}$ and $\Lambda+\overline{\Lambda}$ measurements and underestimates the results for $\pi^\pm$ and K^0_S.

In a similar attempt to the comparison between the v_n measurement and the model calculation in Tab. 3, the performance of these models have been further studied for $v_{n,mk}$ by taking the relative ratios between each model and the measurements of $\pi^\pm$, $K^\pm$ and $p+\bar{p}$. These relative ratios are summarised in Tab. 4 where TRENTo calculations reproduce $v_{4,22}$ slightly better than AMPT. Comparison between Tab.
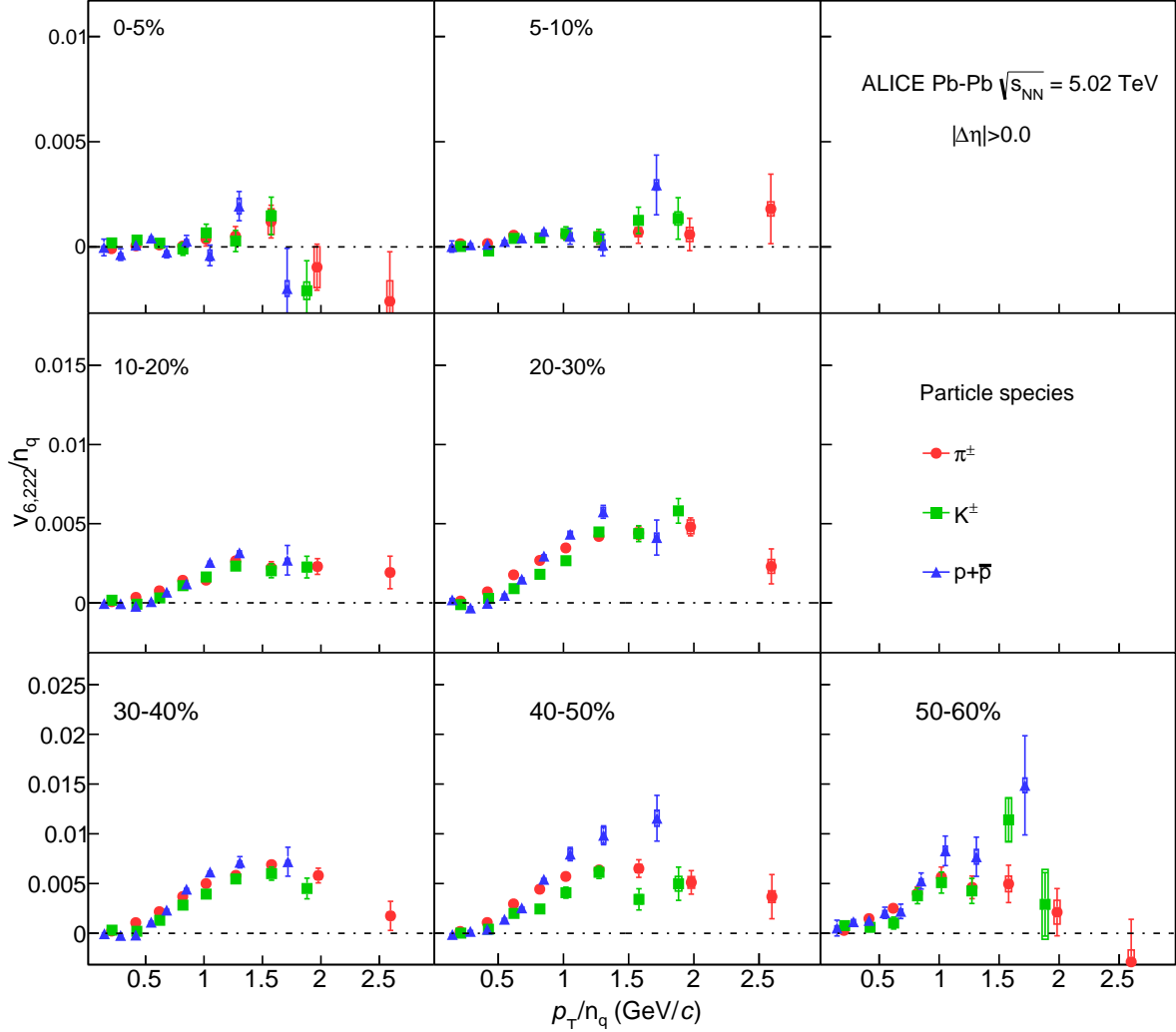
Figure 13: The p_T/n_q-dependence of $v_{6,222}/n_q$ for different particle species grouped into different centrality intervals of Pb–Pb collisions at $\sqrt{s_{NN}} = 5.02$ TeV.

4 and 3 shows that the AMPT calculations reproduces $v_{4,22}$ with ∼20% higher discrepancy on average compared to v_4, and, TRENTo calculations performs equally well for $v_{4,22}$ compared to v_4. It is necessary to stress, however, that the non-linear flow modes have smaller magnitudes with respect to v_n and any discrepancy between the models and the data becomes magnified in the ratios reported in Tab. 4.

For $v_{5,32}$, the comparison seems slightly different, with TRENTo predictions overestimating the measurements for all centrality intervals, while AMPT seemingly reproduces the data better. The AMPT model slightly overestimates the measurements from 0-10% to 20-30% centrality interval. It underestimates the measurements of $\pi^\pm$, $K^\pm$ and $p + \overline{p}$ for more peripheral collisions while it reproduces the measurements of K^0_S and $\Lambda + \overline{\Lambda}$ relatively well up to 40-50% centrality interval. These comparisons are reflected in Table 4 where AMPT performs on average $20 - 27\%$ better than TRENTo for $\pi^\pm$, $K^\pm$ and $p + \overline{p}$.

For $v_{6,33}$, both models reproduce the data at 0-10% centrality interval. For 10-20% up to 30-40% centrality interval, AMPT reproduces the data while TRENTo slightly overestimates the measurements. Finally, comparison with $v_{6,222}$ shows an agreement between both models and the measurements of $\pi^\pm$, $K^\pm$ and
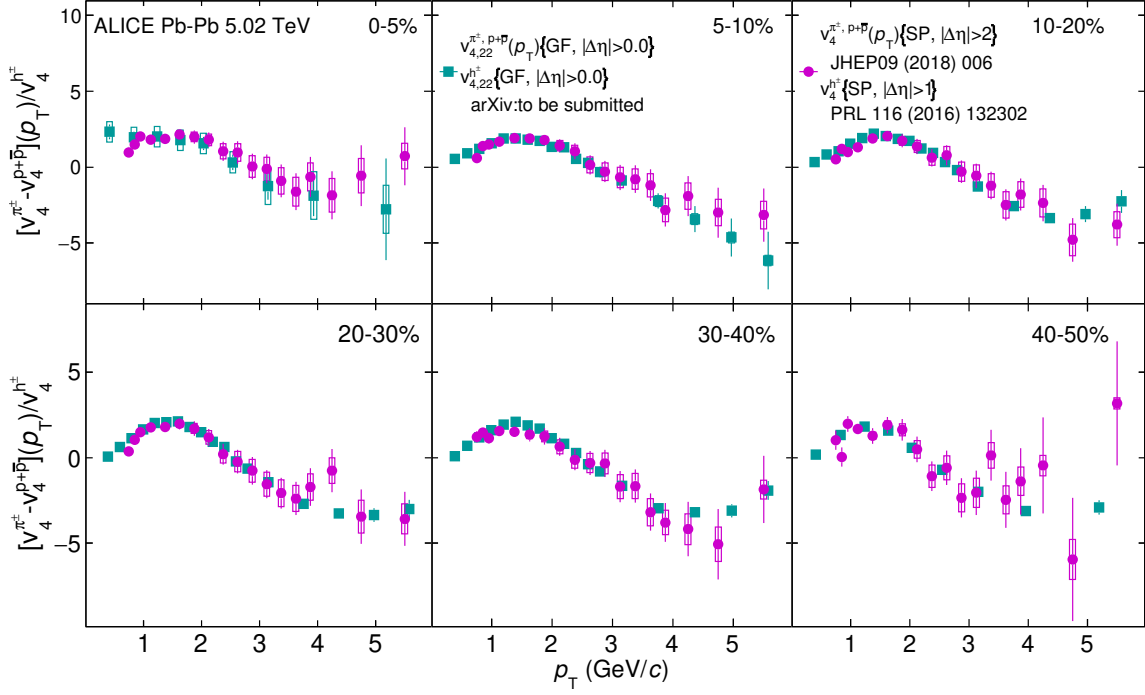
23

Figure 14: The comparison between $[v_{4,22}^{\pi^\pm} - v_{4,22}^{p+\bar{p}}](p_T)/v_{4,22}^{h^\pm}$ and $[v_4^{\pi^\pm} - v_4^{p+\bar{p}}](p_T)/v_4^{h^\pm}$ grouped into different centrality intervals of Pb–Pb collisions at $\sqrt{s_{NN}} = 5.02$ TeV.

p $+ \bar{p}$ at 0-10% up to 30-40% centrality intervals [2].

All in all, this study shows larger difference between the model calculations and the $v_{n,mk}$ measurements with respect to that of v_n, indicating a larger sensitivity to the initial conditions and transport properties for the non-linear flow modes. As a result, it is useful to tune the input parameters of hydrodynamic models considering also the non-linear flow measurements.

---

[2]The ratios reported for $v_{6,33}$ and $v_{6,222}$ in Tab. 4 are not to be taken at face value as the magnitudes of these two non-linear flow modes are almost zero.
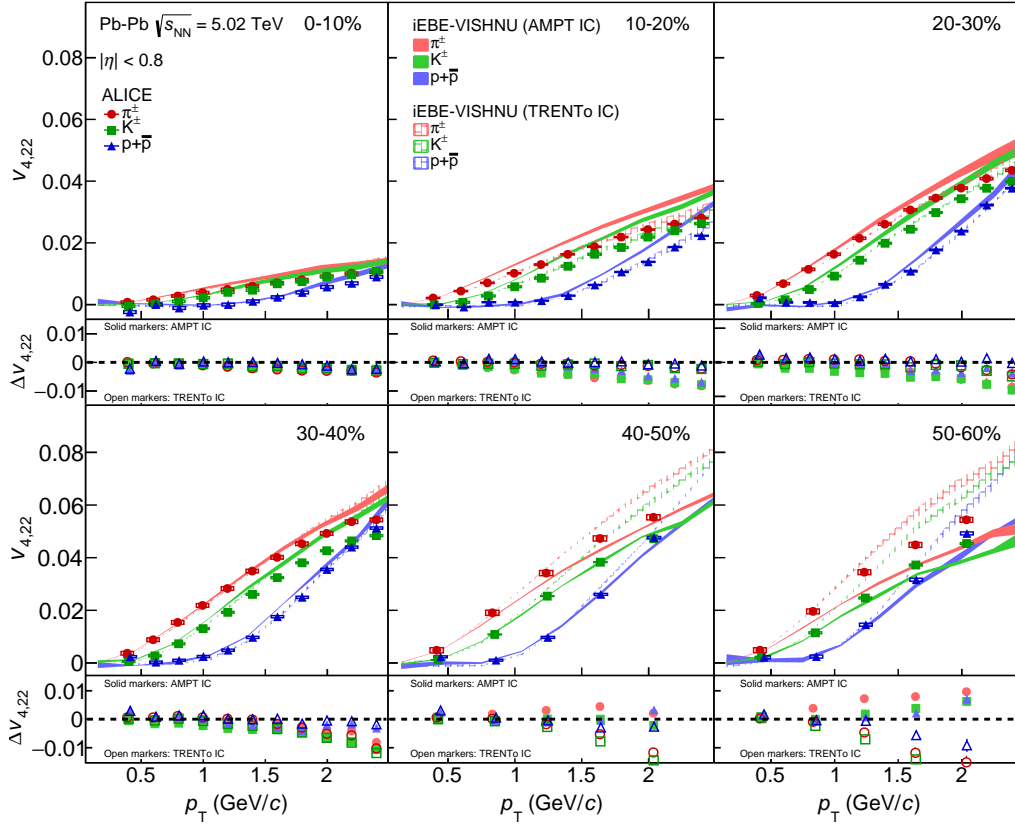
Figure 15: The p_T-differential $v_{4,22}$ for $\pi^\pm$, $K^\pm$ and $p+\overline{p}$ in 0-10% up to 50-60% centrality intervals of Pb–Pb collisions at $\sqrt{s_{NN}} = 5.02$ TeV compared with iEBE-VISHNU hybrid models with two different sets of initial parameters: AMPT initial conditions ($\eta/s = 0.08$ and $\zeta/s = 0$) shown in solid bands and TRENTo initial conditions ($\eta/s(T)$ and $\zeta/s(T)$) in hatched bands. The bottom panels show the difference between the measurements and each model.

7   Summary

In this article, the measurement of non-linear flow modes, $v_{4,22}$, $v_{5,32}$, $v_{6,222}$ and $v_{6,33}$ as a function of transverse momentum for different particle species, i.e. $\pi^\pm$, $K^\pm$, K_S^0, $p+\overline{p}$, $\Lambda+\overline{\Lambda}$ and ϕ-meson are reported for the first time. The results are presented in a wide range of centrality intervals from 0-5% up to 50-60% in Pb–Pb collisions at $\sqrt{s_{NN}} = 5.02$ TeV. The magnitude of non-linear flow modes, $v_{n,mk}$, are obtained with a multi-particle correlation technique, namely the generic framework, selecting the identified hadron under study and the reference flow particles from different, non-overlapping pseudorapidity regions.

The measured $v_{4,22}$, $v_{5,32}$ and $v_{6,222}$ exhibit a distinct centrality dependence. This centrality dependence originates from the contribution of initial state eccentricity, ε_2, as shown in Eq. 5. As expected, $v_{6,33}$ does not exhibit a considerable centrality dependence since ε_3 quantifies primarily the event-by-event fluctuations of the initial energy density profile. This is supported by the relatively large magnitude of $v_{6,33}$ in the most-central collisions (0-5%). A clear mass ordering is observed in the low p_T region ($p_T < 2.5$ GeV/c). A closer comparison between v_4 and $v_{4,22}$ shows that this mass ordering seems slightly larger for $v_{4,22}$ than v_4 at very low p_T ($p_T < 0.8$ GeV/c). In the intermediate p_T region ($p_T > 2.5$ GeV/c), a particle type grouping is observed where the magnitude of non-linear modes for baryons are larger than for mesons similar to observations in v_n measurements. The NCQ scaling holds at an approximate level
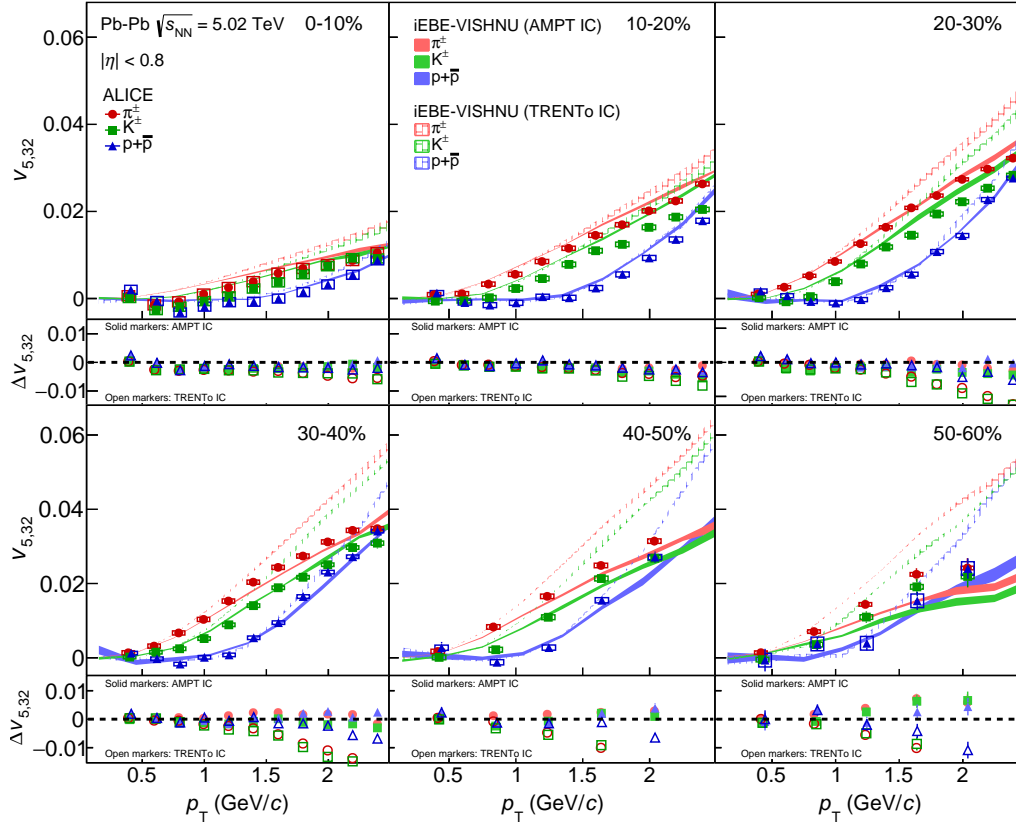
Figure 16: The p_{T}-differential $v_{5,32}$ for $\pi^{\pm}$, $K^{\pm}$ and $p+\bar{p}$ in 0-10% up to 50-60% centrality intervals of Pb–Pb collisions at $\sqrt{s_{\mathrm{NN}}} = 5.02$ TeV compared with iEBE-VISHNU hybrid models with two different sets of initial parameters: AMPT initial conditions ($\eta/s = 0.08$ and $\zeta/s = 0$) shown in solid bands and TRENTo initial conditions ($\eta/s(\mathrm{T})$ and $\zeta/s(\mathrm{T})$) in hatched bands. The bottom panels show the difference between the measurements and each model.

of $\pm 20\%$ within the current level of statistical and systematic uncertainties, similar to that of anisotropic flow coefficients [41].

The comparison of two models based on the iEBE-VISHNU hybrid model, and with two different initial conditions (AMPT and TRENTo) and transport properties show that neither of the models are able to fully describe the measurements. This varies depending on the centrality percentile and particle species similar to the model-data comparison for anisotropic flow coefficients [41]. Measurements are better predicted by the models in more central collisions. All in all, the model using AMPT initial conditions ($\eta/s = 0.08$ and $\zeta/s = 0$) exhibits a magnitude and shape closer to the measurements. As a result, in order to further constrain the values of transport properties and the initial conditions of the system, it is necessary to tune the input parameters of future hydrodynamic calculations attempting to describe these measurements.
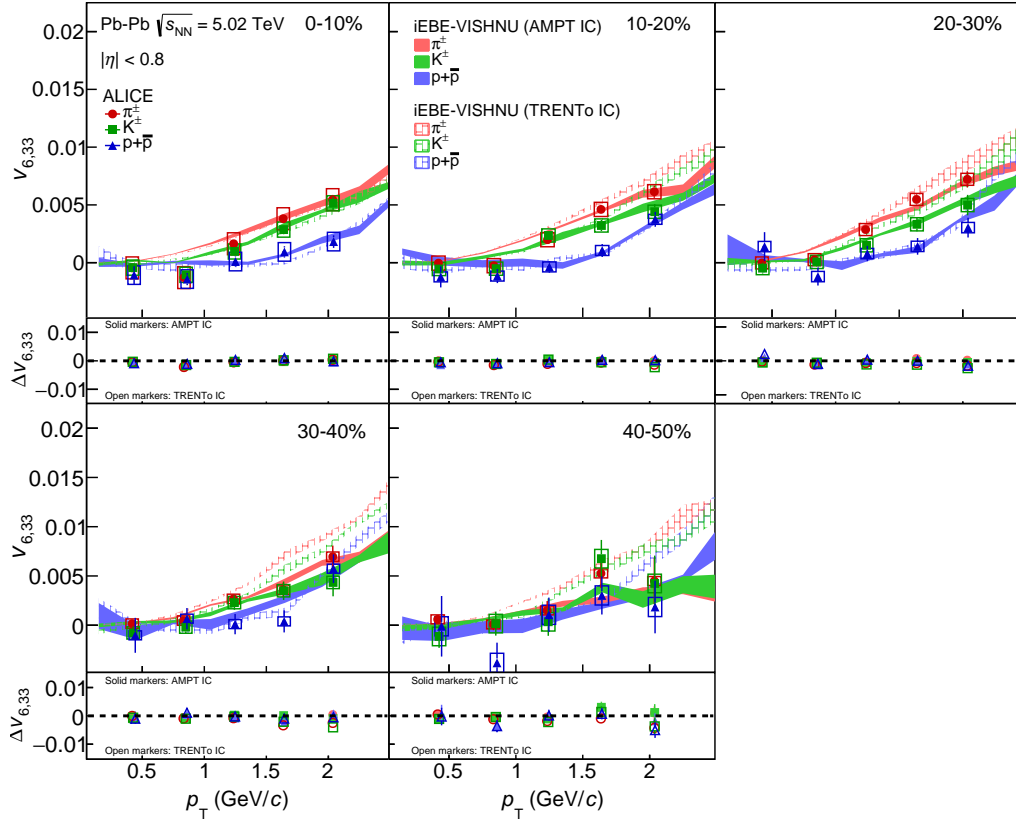
Acknowledgements

Figure 17: The p_T-differential $v_{6,33}$ for $\pi^\pm$, $K^\pm$ and $p+\bar{p}$ in 0-10% up to 40-50% centrality intervals of Pb–Pb collisions at $\sqrt{s_{NN}} = 5.02$ TeVcompared with iEBE-VISHNU hybrid models with two different sets of initial parameters: AMPT initial conditions ($\eta/s = 0.08$ and $\zeta/s = 0$) shown in solid bands and TRENTo initial conditions ($\eta/s(T)$ and $\zeta/s(T)$) in hatched bands. The bottom panels show the difference between the measurements and each model.

References

[1] S. Borsanyi, G. Endrodi, Z. Fodor, A. Jakovac, S. D. Katz, S. Krieg, C. Ratti, and K. K. Szabo, "The QCD equation of state with dynamical quarks", *JHEP* **11** (2010) , arXiv:1007.2580 [hep-lat].

[2] T. Bhattacharya *et al.*, "QCD Phase Transition with Chiral Quarks and Physical Quark Masses", *Phys. Rev. Lett.* **113** no. 8, (2014) , arXiv:1402.5175 [hep-lat].

[3] E. V. Shuryak, "Theory and phenomenology of the QCD vacuum", *Phys. Rept.* **115** (1984) .

[4] J. Cleymans, R. V. Gavai, and E. Suhonen, "Quarks and Gluons at High Temperatures and Densities", *Phys. Rept.* **130** (1986) .

[5] S. A. Bass, M. Gyulassy, H. Stoecker, and W. Greiner, "Signatures of quark gluon plasma formation in high-energy heavy ion collisions: A Critical review", *J. Phys.* **G25** (1999) , arXiv:hep-ph/9810281 [hep-ph].

[6] M. Miller and R. Snellings, "Eccentricity fluctuations and its possible effect on elliptic flow measurements", arXiv:nucl-ex/0312008 [nucl-ex].
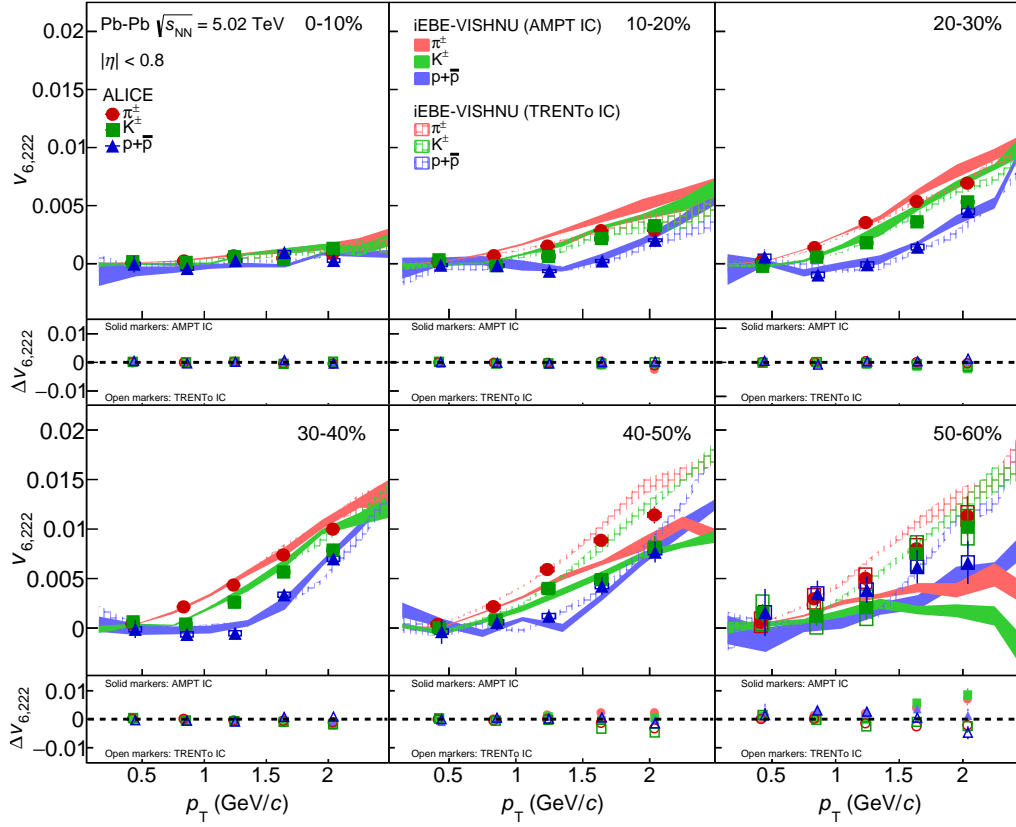
Figure 18: The p_{T}-differential $v_{6,222}$ for $\pi^{\pm}$, $K^{\pm}$ and $p+\bar{p}$ in 0-10% up to 50-60% centrality intervals of Pb–Pb collisions at $\sqrt{s_{NN}} = 5.02$ TeVcompared with iEBE-VISHNU hybrid models with two different sets of initial parameters: AMPT initial conditions ($\eta/s = 0.08$ and $\zeta/s = 0$) shown in solid bands and TRENTo initial conditions ($\eta/s(\mathrm{T})$ and $\zeta/s(\mathrm{T})$) in hatched bands. The bottom panels show the difference between the measurements and each model.

[7] R. S. Bhalerao and J.-Y. Ollitrault, "Eccentricity fluctuations and elliptic flow at RHIC", *Phys. Lett.* **B641** (2006) , arXiv:nucl-th/0607009 [nucl-th].

[8] B. Alver *et al.*, "Importance of correlations and fluctuations on the initial source eccentricity in high-energy nucleus-nucleus collisions", *Phys. Rev.* **C77** (2008) , arXiv:0711.3724 [nucl-ex].

[9] B. Alver and G. Roland, "Collision geometry fluctuations and triangular flow in heavy-ion collisions", *Phys. Rev.* **C81** (2010) , arXiv:1003.0194 [nucl-th]. [Erratum: Phys. Rev.C82,039903(2010)].

[10] B. H. Alver, C. Gombeaud, M. Luzum, and J.-Y. Ollitrault, "Triangular flow in hydrodynamics and transport theory", *Phys. Rev.* **C82** (2010) , arXiv:1007.5469 [nucl-th].

[11] **PHOBOS** Collaboration, S. Manly *et al.*, "System size, energy and pseudorapidity dependence of directed and elliptic flow at RHIC", *Nucl. Phys.* **A774** (2006) , arXiv:nucl-ex/0510031 [nucl-ex].

[12] S. A. Voloshin, "Toward the energy and the system size dependece of elliptic flow: Working on flow fluctuations", in *22nd Winter Workshop on Nuclear Dynamics (WWND 2006) La Jolla, California, March 11-19, 2006*. 2006. arXiv:nucl-th/0606022 [nucl-th].
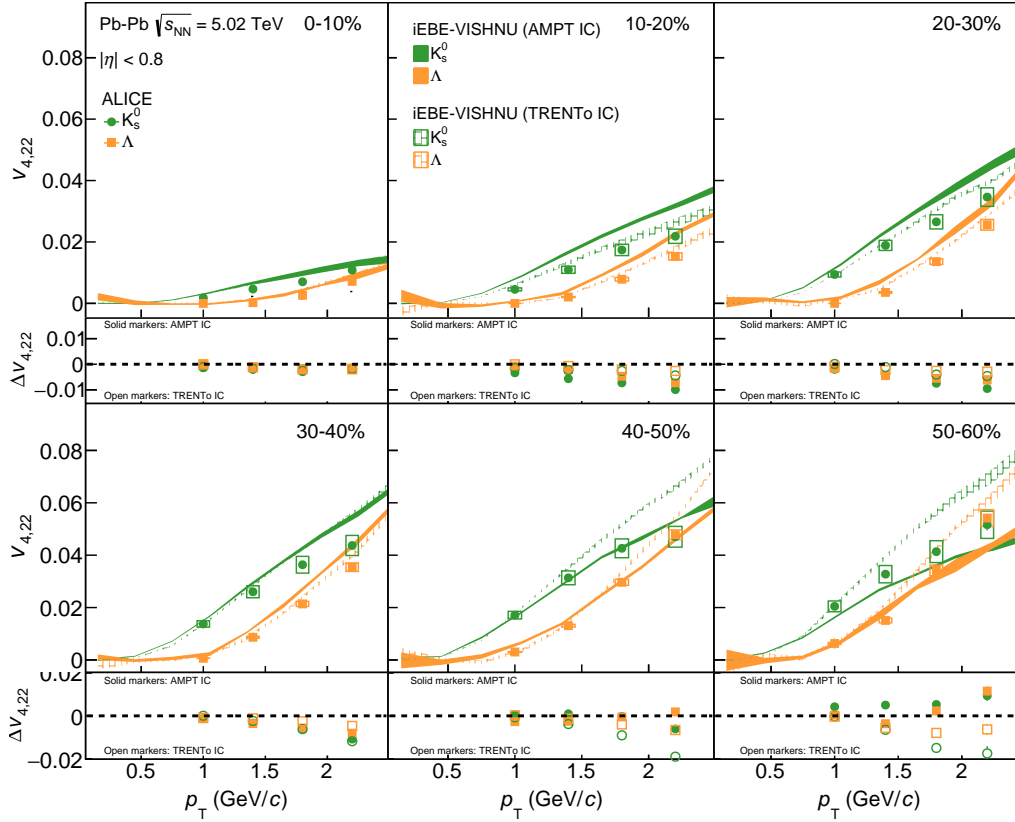
Figure 19: The p_T-differential $v_{4,22}$ for K_S^0 and $\Lambda + \overline{\Lambda}$ in 0-10% up to 50-60% centrality intervals of Pb–Pb collisions at $\sqrt{s_{NN}} = 5.02$ TeVcompared with iEBE-VISHNU hybrid models with two different sets of initial parameters: AMPT initial conditions (η/s= 0.08 and $\zeta/s = 0$) shown in solid bands and TRENTo initial conditions (η/s(T) and ζ/s(T)) in hatched bands. The bottom panels show the difference between the measurements and each model.

[13] S. Voloshin and Y. Zhang, "Flow study in relativistic nuclear collisions by Fourier expansion of Azimuthal particle distributions", *Z. Phys.* **C70** (1996) , arXiv:hep-ph/9407282 [hep-ph].

[14] **STAR** Collaboration, J. Adams *et al.*, "Particle type dependence of azimuthal anisotropy and nuclear modification of particle production in Au + Au collisions at $\sqrt{s_{NN}}$ =200 GeV", *Phys. Rev. Lett.* **92** (2004) , arXiv:nucl-ex/0306007 [nucl-ex].

[15] **STAR** Collaboration, B. I. Abelev *et al.*, "Mass, quark-number, and $\sqrt{s_{NN}}$ dependence of the second and fourth flow harmonics in ultra-relativistic nucleus-nucleus collisions", *Phys. Rev.* **C75** (2007) , arXiv:nucl-ex/0701010 [nucl-ex].

[16] **PHENIX** Collaboration, S. S. Adler *et al.*, "Elliptic flow of identified hadrons in Au+Au collisions at $\sqrt{s_{NN}}$ =200 GeV", *Phys. Rev. Lett.* **91** (2003) , arXiv:nucl-ex/0305013 [nucl-ex].

[17] **PHENIX** Collaboration, A. Adare *et al.*, "Scaling properties of azimuthal anisotropy in Au+Au and Cu+Cu collisions at s(NN) = 200-GeV", *Phys. Rev. Lett.* **98** (2007) , arXiv:nucl-ex/0608033 [nucl-ex].

[18] **PHOBOS** Collaboration, B. Alver *et al.*, "Event-by-Event Fluctuations of Azimuthal Particle Anisotropy in Au + Au Collisions at $\sqrt{s_{NN}}$ = 200 GeV", *Phys. Rev. Lett.* **104** (2010) , arXiv:nucl-ex/0702036 [nucl-ex].
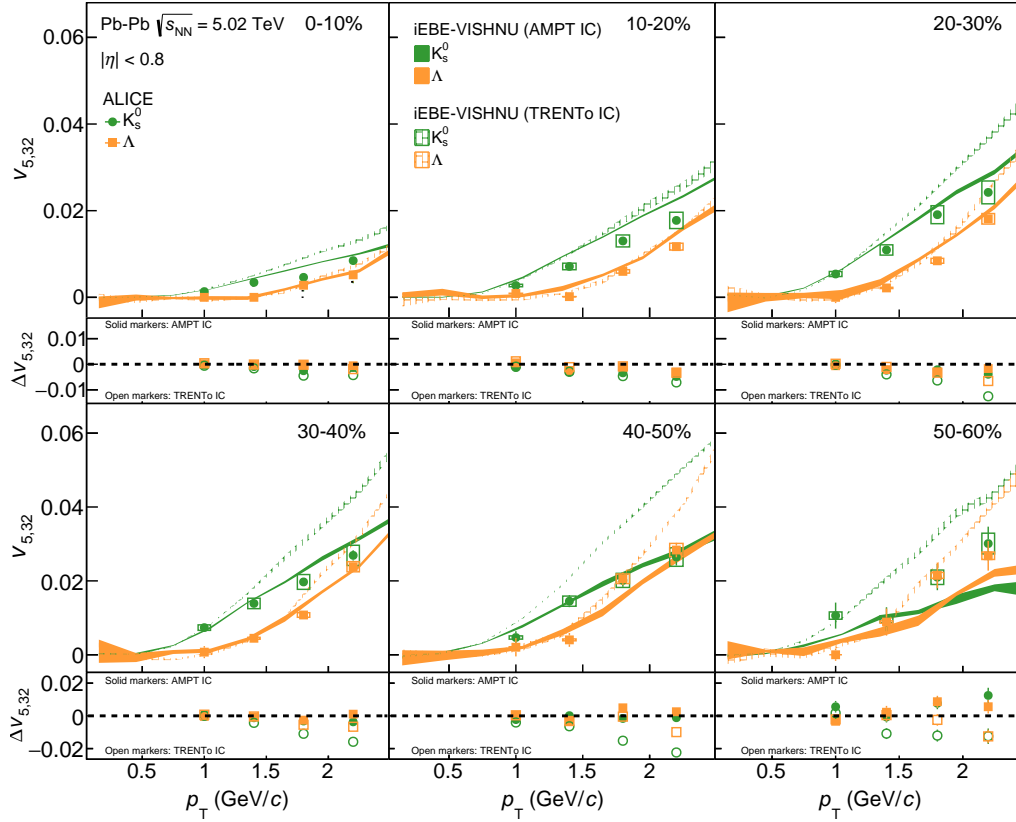
Figure 20: The p_{T}-differential $v_{5,32}$ for K_S^0 and $\Lambda + \overline{\Lambda}$ in 0-10% up to 50-60% centrality intervals of Pb–Pb collisions at $\sqrt{s_{\mathrm{NN}}} = 5.02$ TeVcompared with iEBE-VISHNU hybrid models with two different sets of initial parameters: AMPT initial conditions ($\eta/s = 0.08$ and $\zeta/s = 0$) shown in solid bands and TRENTo initial conditions ($\eta/s(\mathrm{T})$ and $\zeta/s(\mathrm{T})$) in hatched bands. The bottom panels show the difference between the measurements and each model.

[19] **PHENIX** Collaboration, K. Adcox *et al.*, "Flow measurements via two particle azimuthal correlations in Au+Au collisions at s(NN)**(1/2) = 130-GeV", *Phys. Rev. Lett.* **89** (2002) , arXiv:nucl-ex/0204005 [nucl-ex].

[20] **STAR** Collaboration, L. Adamczyk *et al.*, "Elliptic flow of identified hadrons in Au+Au collisions at $\sqrt{s_{NN}} = 7.7$-62.4 GeV", *Phys. Rev.* **C88** (2013) , arXiv:1301.2348 [nucl-ex].

[21] **PHENIX** Collaboration, S. S. Adler *et al.*, "Saturation of azimuthal anisotropy in Au + Au collisions at s(NN)**(1/2) 62-GeV to 200-GeV", *Phys. Rev. Lett.* **94** (2005) , arXiv:nucl-ex/0411040 [nucl-ex].

[22] **PHENIX** Collaboration, S. Afanasiev *et al.*, "Systematic Studies of Elliptic Flow Measurements in Au+Au Collisions at s**(1/2) = 200-GeV", *Phys. Rev.* **C80** (2009) , arXiv:0905.1070 [nucl-ex].

[23] **PHENIX** Collaboration, A. Adare *et al.*, "Measurements of Higher-Order Flow Harmonics in Au+Au Collisions at $\sqrt{s_{NN}} = 200$ GeV", *Phys. Rev. Lett.* **107** (2011) , arXiv:1105.3928 [nucl-ex].

[24] **STAR** Collaboration, K. H. Ackermann *et al.*, "Elliptic flow in Au + Au collisions at (S(NN))**(1/2) = 130 GeV", *Phys. Rev. Lett.* **86** (2001) , arXiv:nucl-ex/0009011 [nucl-ex].
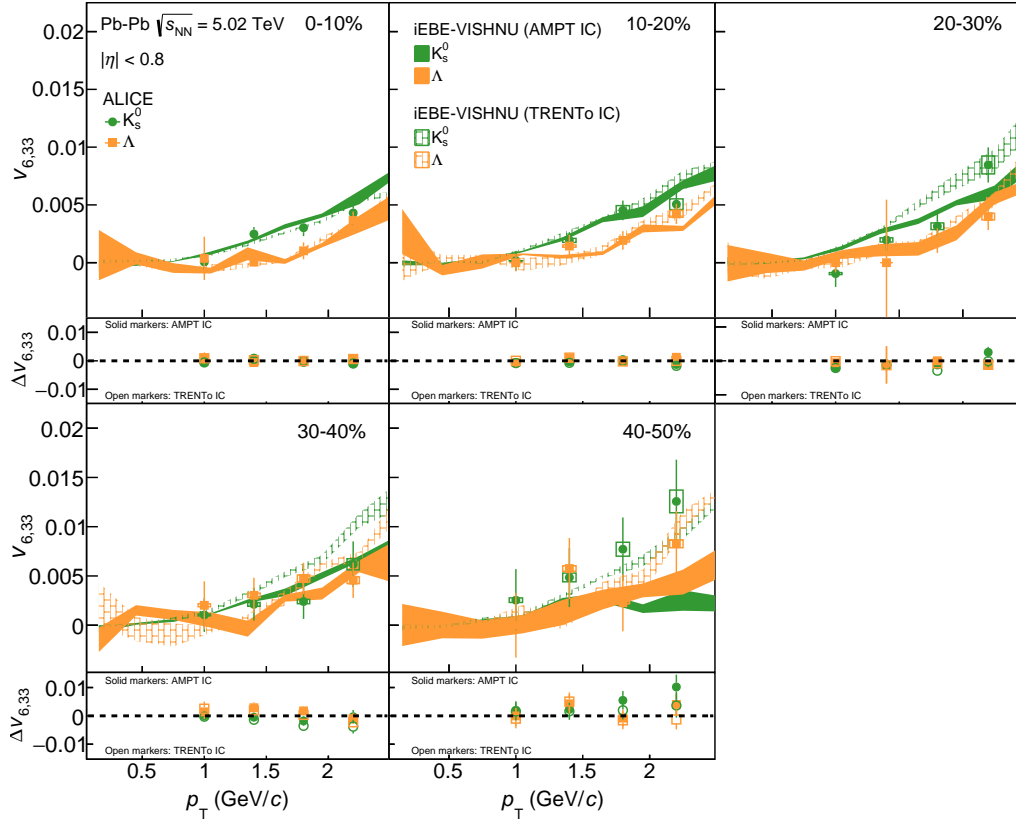
Figure 21: The p_T-differential $v_{6,33}$ for K_S^0 and $\Lambda + \overline{\Lambda}$ in 0-10% up to 40-50% centrality intervals of Pb–Pb collisions at $\sqrt{s_{NN}} = 5.02$ TeVcompared with iEBE-VISHNU hybrid models with two different sets of initial parameters: AMPT initial conditions ($\eta/s = 0.08$ and $\zeta/s = 0$) shown in solid bands and TRENTo initial conditions ($\eta/s(T)$ and $\zeta/s(T)$) in hatched bands. The bottom panels show the difference between the measurements and each model.

[25] **STAR** Collaboration, C. Adler *et al.*, "Identified particle elliptic flow in Au + Au collisions at s(NN)**(1/2) = 130-GeV", *Phys. Rev. Lett.* **87** (2001) , arXiv:nucl-ex/0107003 [nucl-ex].

[26] **STAR** Collaboration, C. Adler *et al.*, "Azimuthal anisotropy and correlations in the hard scattering regime at RHIC", *Phys. Rev. Lett.* **90** (2003) , arXiv:nucl-ex/0206006 [nucl-ex].

[27] **STAR** Collaboration, C. Adler *et al.*, "Elliptic flow from two and four particle correlations in Au+Au collisions at $\sqrt{s_{NN}} = 130$ GeV", *Phys. Rev.* **C66** (2002) , arXiv:nucl-ex/0206001 [nucl-ex].

[28] **STAR** Collaboration, J. Adams *et al.*, "Azimuthal anisotropy at RHIC: The First and fourth harmonics", *Phys. Rev. Lett.* **92** (2004) , arXiv:nucl-ex/0310029 [nucl-ex].

[29] **STAR** Collaboration, J. Adams *et al.*, "Azimuthal anisotropy and correlations at large transverse momenta in p+p and Au+Au collisions at $\sqrt{s_{NN}} = 200$ GeV", *Phys. Rev. Lett.* **93** (2004) , arXiv:nucl-ex/0407007 [nucl-ex].

[30] **STAR** Collaboration, J. Adams *et al.*, "Azimuthal anisotropy in Au+Au collisions at s(NN)**(1/2) = 200-GeV", *Phys. Rev.* **C72** (2005) , arXiv:nucl-ex/0409033 [nucl-ex].

[31] **ALICE** Collaboration, K. Aamodt *et al.*, "Elliptic flow of charged particles in Pb-Pb collisions at 2.76 TeV", *Phys. Rev. Lett.* **105** (2010) , `arXiv:1011.3914 [nucl-ex]`.

[32] **ALICE** Collaboration, K. Aamodt *et al.*, "Higher harmonic anisotropic flow measurements of charged particles in Pb-Pb collisions at $\sqrt{s_{NN}}$=2.76 TeV", *Phys. Rev. Lett.* **107** (2011) , `arXiv:1105.3865 [nucl-ex]`.

[33] **ALICE** Collaboration, B. Abelev *et al.*, "Anisotropic flow of charged hadrons, pions and (anti-)protons measured at high transverse momentum in Pb-Pb collisions at $\sqrt{s_{NN}}$=2.76 TeV", *Phys. Lett.* **B719** (2013) , `arXiv:1205.5761 [nucl-ex]`.

[34] **CMS** Collaboration, S. Chatrchyan *et al.*, "Azimuthal anisotropy of charged particles at high transverse momenta in PbPb collisions at $\sqrt{s_{NN}} = 2.76$ TeV", *Phys. Rev. Lett.* **109** (2012) , `arXiv:1204.1850 [nucl-ex]`.

[35] **CMS** Collaboration, S. Chatrchyan *et al.*, "Measurement of the elliptic anisotropy of charged particles produced in PbPb collisions at $\sqrt{s_{NN}}$=2.76 TeV", *Phys. Rev.* **C87** no. 1, (2013) , `arXiv:1204.1409 [nucl-ex]`.

[36] **ATLAS** Collaboration, G. Aad *et al.*, "Measurement of the pseudorapidity and transverse momentum dependence of the elliptic flow of charged particles in lead-lead collisions at $\sqrt{s_{NN}} = 2.76$ TeV with the ATLAS detector", *Phys. Lett.* **B707** (2012) , `arXiv:1108.6018 [hep-ex]`.

[37] **ATLAS** Collaboration, G. Aad *et al.*, "Measurement of the azimuthal anisotropy for charged particle production in $\sqrt{s_{NN}} = 2.76$ TeV lead-lead collisions with the ATLAS detector", *Phys. Rev.* **C86** (2012) , `arXiv:1203.3087 [hep-ex]`.

[38] **ALICE** Collaboration, B. B. Abelev *et al.*, "Elliptic flow of identified hadrons in Pb-Pb collisions at $\sqrt{s_{NN}} = 2.76$ TeV", *JHEP* **06** (2015) , `arXiv:1405.4632 [nucl-ex]`.

[39] **ALICE** Collaboration, J. Adam *et al.*, "Higher harmonic flow coefficients of identified hadrons in Pb-Pb collisions at $\sqrt{s_{NN}} = 2.76$ TeV", *JHEP* **09** (2016) , `arXiv:1606.06057 [nucl-ex]`.

[40] **ALICE** Collaboration, J. Adam *et al.*, "Anisotropic flow of charged particles in Pb-Pb collisions at $\sqrt{s_{NN}} = 5.02$ TeV", *Phys. Rev. Lett.* **116** no. 13, (2016) , `arXiv:1602.01119 [nucl-ex]`.

[41] **ALICE** Collaboration, S. Acharya *et al.*, "Anisotropic flow of identified particles in Pb-Pb collisions at $\sqrt{s_{NN}} = 5.02$ TeV", *JHEP* **09** (2018) , `arXiv:1805.04390 [nucl-ex]`.

[42] **CMS** Collaboration, S. Chatrchyan *et al.*, "Measurement of higher-order harmonic azimuthal anisotropy in PbPb collisions at $\sqrt{s_{NN}} = 2.76$ TeV", *Phys. Rev.* **C89** no. 4, (2014) , `arXiv:1310.8651 [nucl-ex]`.

[43] **ALICE** Collaboration, J. Adam *et al.*, "Event shape engineering for inclusive spectra and elliptic flow in Pb-Pb collisions at $\sqrt{s_{NN}} = 2.76$ TeV", *Phys. Rev.* **C93** no. 3, (2016) , `arXiv:1507.06194 [nucl-ex]`.

[44] **ALICE** Collaboration, S. Acharya *et al.*, "Energy dependence and fluctuations of anisotropic flow in Pb-Pb collisions at $\sqrt{s_{NN}} = 5.02$ and 2.76 TeV", *JHEP* **07** (2018) , `arXiv:1804.02944 [nucl-ex]`.

[45] **ALICE** Collaboration, S. Acharya *et al.*, "Anisotropic flow in Xe-Xe collisions at $\sqrt{s_{NN}} = $ **5.44** TeV", *Phys. Lett.* **B784** (2018) , `arXiv:1805.01832 [nucl-ex]`.

[46] P. Kovtun, D. T. Son, and A. O. Starinets, "Viscosity in strongly interacting quantum field theories from black hole physics", *Phys. Rev. Lett.* **94** (2005) , arXiv:hep-th/0405231 [hep-th].

[47] H. Niemi, K. J. Eskola, R. Paatelainen, and K. Tuominen, "Predictions for 5.023 TeV Pb + Pb collisions at the CERN Large Hadron Collider", *Phys. Rev.* **C93** no. 1, (2016) , arXiv:1511.04296 [hep-ph].

[48] D. Teaney and L. Yan, "Triangularity and Dipole Asymmetry in Heavy Ion Collisions", *Phys. Rev.* **C83** (2011) , arXiv:1010.1876 [nucl-th].

[49] D. Teaney and L. Yan, "Event-plane correlations and hydrodynamic simulations of heavy ion collisions", *Phys. Rev.* **C90** no. 2, (2014) , arXiv:1312.3689 [nucl-th].

[50] J. Qian, U. Heinz, R. He, and L. Huo, "Differential flow correlations in relativistic heavy-ion collisions", *Phys. Rev.* **C95** no. 5, (2017) , arXiv:1703.04077 [nucl-th].

[51] R. S. Bhalerao, J.-Y. Ollitrault, and S. Pal, "Characterizing flow fluctuations with moments", *Phys. Lett.* **B742** (2015) , arXiv:1411.5160 [nucl-th].

[52] L. Yan and J.-Y. Ollitrault, "v_4, v_5, v_6, v_7: nonlinear hydrodynamic response versus LHC data", *Phys. Lett.* **B744** (2015) , arXiv:1502.02502 [nucl-th].

[53] **ALICE** Collaboration, S. Acharya *et al.*, "Linear and non-linear flow modes in Pb-Pb collisions at $\sqrt{s_{NN}} = 2.76$ TeV", *Phys. Lett.* **B773** (2017) , arXiv:1705.04377 [nucl-ex].

[54] **ALICE** Collaboration, S. Acharya *et al.*, "Systematic studies of correlations between different order flow harmonics in Pb-Pb collisions at $\sqrt{s_{NN}} = 2.76$ TeV", *Phys. Rev.* **C97** no. 2, (2018) , arXiv:1709.01127 [nucl-ex].

[55] S. A. Voloshin, A. M. Poskanzer, and R. Snellings, "Collective phenomena in non-central nuclear collisions", arXiv:0809.2949 [nucl-ex].

[56] S. A. Voloshin, "Transverse radial expansion and directed flow", *Phys. Rev.* **C55** (1997) , arXiv:nucl-th/9611038 [nucl-th].

[57] P. Huovinen, P. F. Kolb, U. W. Heinz, P. V. Ruuskanen, and S. A. Voloshin, "Radial and elliptic flow at RHIC: Further predictions", *Phys. Lett.* **B503** (2001) , arXiv:hep-ph/0101136 [hep-ph].

[58] S. A. Voloshin, "Anisotropic flow", *Nucl. Phys.* **A715** (2003) , arXiv:nucl-ex/0210014 [nucl-ex].

[59] D. Molnar and S. A. Voloshin, "Elliptic flow at large transverse momenta from quark coalescence", *Phys. Rev. Lett.* **91** (2003) , arXiv:nucl-th/0302014 [nucl-th].

[60] **PHENIX** Collaboration, A. Adare *et al.*, "Deviation from quark-number scaling of the anisotropy parameter v_2 of pions, kaons, and protons in Au+Au collisions at $\sqrt{s_{NN}} = 200$ GeV", *Phys. Rev.* **C85** (2012) , arXiv:1203.2644 [nucl-ex].

[61] X. Zhu, Y. Zhou, H. Xu, and H. Song, "Correlations of flow harmonics in 2.76A TeV Pb–Pb collisions", *Phys. Rev.* **C95** no. 4, (2017) , arXiv:1608.05305 [nucl-th].

[62] **ALICE** Collaboration, K. Aamodt *et al.*, "The ALICE experiment at the CERN LHC", *JINST* **3** (2008) .

[63] **ALICE** Collaboration, B. B. Abelev *et al.*, "Performance of the ALICE Experiment at the CERN LHC", *Int. J. Mod. Phys.* **A29** (2014) , arXiv:1402.4476 [nucl-ex].

[64] **ALICE** Collaboration, K. Aamodt *et al.*, "Charged-particle multiplicity density at mid-rapidity in central Pb-Pb collisions at $\sqrt{s_{NN}} = 2.76$ TeV", *Phys. Rev. Lett.* **105** (2010) , `arXiv:1011.3916` `[nucl-ex]`.

[65] J. Alme *et al.*, "The ALICE TPC, a large 3-dimensional tracking device with fast readout for ultra-high multiplicity events", *Nucl. Instrum. Meth.* **A622** (2010) , `arXiv:1001.1950` `[physics.ins-det]`.

[66] **ALICE** Collaboration, E. Abbas *et al.*, "Performance of the ALICE VZERO system", *JINST* **8** (2013) , `arXiv:1306.3130` `[nucl-ex]`.

[67] **ALICE** Collaboration, B. Abelev *et al.*, "Centrality determination of Pb-Pb collisions at $\sqrt{s_{NN}} = 2.76$ TeV with ALICE", *Phys. Rev.* **C88** no. 4, (2013) , `arXiv:1301.4361` `[nucl-ex]`.

[68] P. Billoir, "Track Fitting With Multiple Scattering: A New Method", *Nucl. Instrum. Meth.* **A225** (1984) .

[69] P. Billoir, R. Fruhwirth, and M. Regler, "TRACK ELEMENT MERGING STRATEGY AND VERTEX FITTING IN COMPLEX MODULAR DETECTORS", *Nucl. Instrum. Meth.* **A241** (1985) .

[70] **ALICE** Collaboration, B. Abelev *et al.*, "Centrality dependence of π, K, p production in Pb-Pb collisions at $\sqrt{s_{NN}} = 2.76$ TeV", *Phys. Rev.* **C88** (2013) , `arXiv:1303.0737` `[hep-ex]`.

[71] K. Olive, "Review of particle physics", *Chinese Physics C* **40** no. 10, (Oct, 2016) .

[72] J. Podolanski and R. Armenteros, "Iii. analysis of v-events", *The London, Edinburgh, and Dublin Philosophical Magazine and Journal of Science* **45** no. 360, (1954) .

[73] **ALICE** Collaboration, J. Adam *et al.*, "Particle identification in ALICE: a Bayesian approach", `arXiv:1602.01392` `[physics.data-an]`.

[74] R. Barlow, "Systematic errors: Facts and fictions", in *Advanced Statistical Techniques in Particle Physics. Proceedings, Conference, Durham, UK, March 18-22, 2002*, pp. 134–144. 2002. `arXiv:hep-ex/0207026` `[hep-ex]`. `http://www.ippp.dur.ac.uk/Workshops/02/statistics/proceedings//barlow.pdf`.

[75] C. Shen, U. Heinz, P. Huovinen, and H. Song, "Radial and elliptic flow in Pb+Pb collisions at the Large Hadron Collider from viscous hydrodynamic", *Phys. Rev.* **C84** (2011) , `arXiv:1105.3226` `[nucl-th]`.

[76] H.-J. Xu, Z. Li, and H. Song, "High order flow harmonics of identified hadrons in 2.76 A TeV Pb+Pb collisions", `arXiv:1602.02029` `[nucl-th]`.

[77] S. McDonald, C. Shen, F. Fillion-Gourdeau, S. Jeon, and C. Gale, "Hydrodynamic predictions for Pb+Pb collisions at 5.02 TeV", *Phys. Rev.* **C95** no. 6, (2017) , `arXiv:1609.02958` `[hep-ph]`.

[78] W. Zhao, H.-j. Xu, and H. Song, "Collective flow in 2.76 A TeV and 5.02 A TeV Pb+Pb collisions", *Eur. Phys. J.* **C77** no. 9, (2017) , `arXiv:1703.10792` `[nucl-th]`.

[79] C. Shen, Z. Qiu, H. Song, J. Bernhard, S. Bass, and U. Heinz, "The iEBE-VISHNU code package for relativistic heavy-ion collisions", *Comput. Phys. Commun.* **199** (2016) , `arXiv:1409.8164` `[nucl-th]`.

[80] H. Song, S. A. Bass, and U. Heinz, "Viscous QCD matter in a hybrid hydrodynamic+Boltzmann approach", *Phys. Rev.* **C83** (2011) , `arXiv:1012.0555` `[nucl-th]`.

[81] H. Song and U. W. Heinz, "Suppression of elliptic flow in a minimally viscous quark-gluon plasma", *Phys. Lett.* **B658** (2008) , `arXiv:0709.0742 [nucl-th]`.

[82] Z.-W. Lin, C. M. Ko, B.-A. Li, B. Zhang, and S. Pal, "A Multi-phase transport model for relativistic heavy ion collisions", *Phys. Rev.* **C72** (2005) , `arXiv:nucl-th/0411110 [nucl-th]`.

[83] J. S. Moreland, J. E. Bernhard, and S. A. Bass, "Alternative ansatz to wounded nucleon and binary collision scaling in high-energy nuclear collisions", *Phys. Rev.* **C92** no. 1, (2015) , `arXiv:1412.4708 [nucl-th]`.

[84] J. E. Bernhard, J. S. Moreland, S. A. Bass, J. Liu, and U. Heinz, "Applying Bayesian parameter estimation to relativistic heavy-ion collisions: simultaneous characterization of the initial state and quark-gluon plasma medium", *Phys. Rev.* **C94** no. 2, (2016) , `arXiv:1605.03954 [nucl-th]`.

A   Additional figures

A.1   KE$_T$ scaling

One suggestion to further study the scaling properties of flow coefficients was to extend the scaling to lower p_T values by studying the transverse kinetic energy dependence of anisotropic flow harmonics. Transverse kinetic energy is defined as $KE_T = m_T - m_0$, where $m_T = \sqrt{m_0^2 + p_T^2}$ is the transverse mass. Figures A.1, A.2, A.3 and A.4 present KE_T scaling for $v_{4,22}$, $v_{5,32}$, $v_{6,33}$ and $v_{6,222}$ respectively, for $\pi^\pm$, $K^\pm$, $p + \overline{p}$, K_S^0, $\Lambda + \overline{\Lambda}$ and ϕ-meson grouped in different centrality intervals.
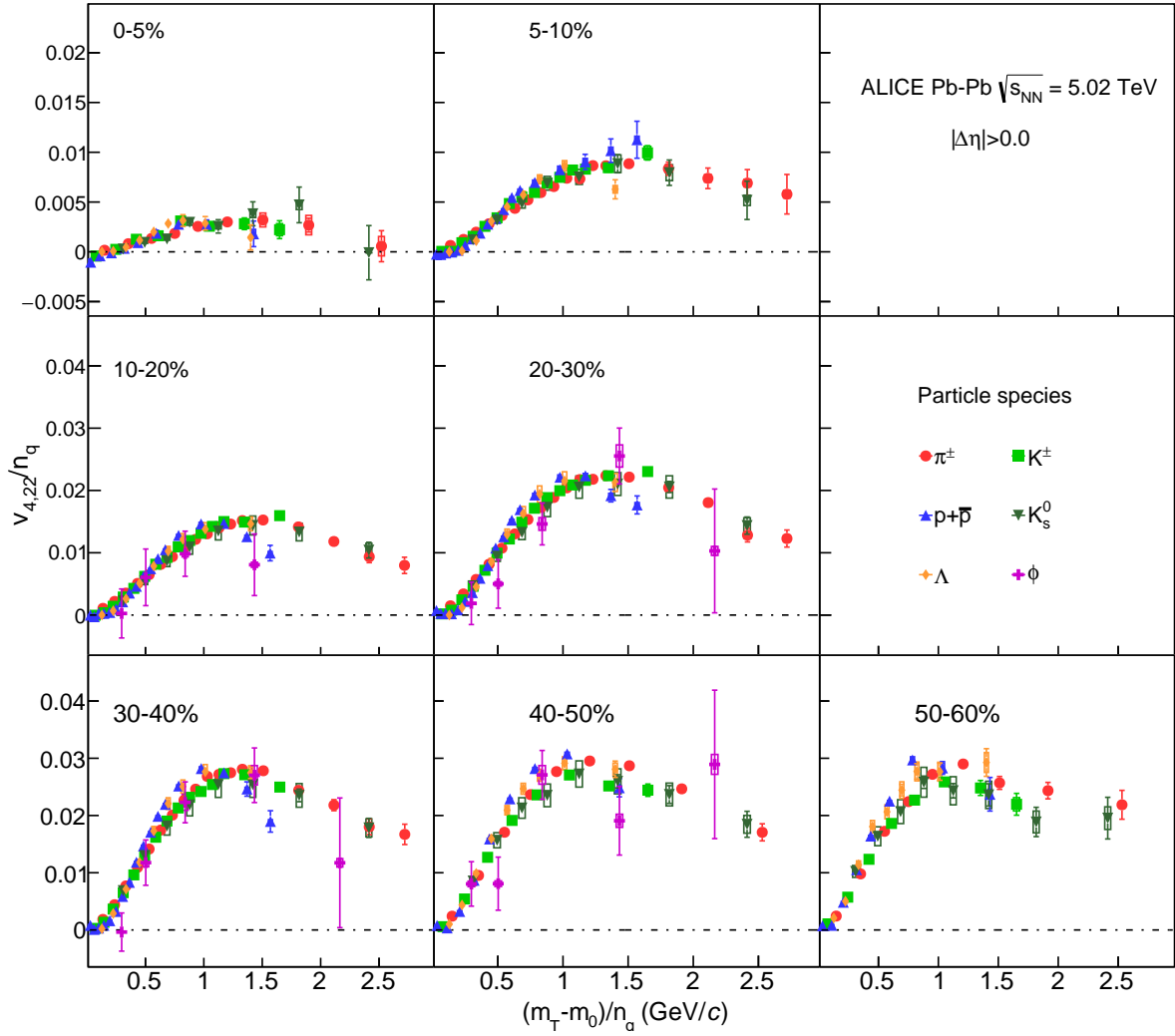
Figure A.1: The $(m_T - m_0)/n_q$-dependence of $v_{4,22}/n_q$ for different particle species grouped into different centrality intervals of Pb–Pb collisions $\sqrt{s_{NN}} = 5.02$ TeV
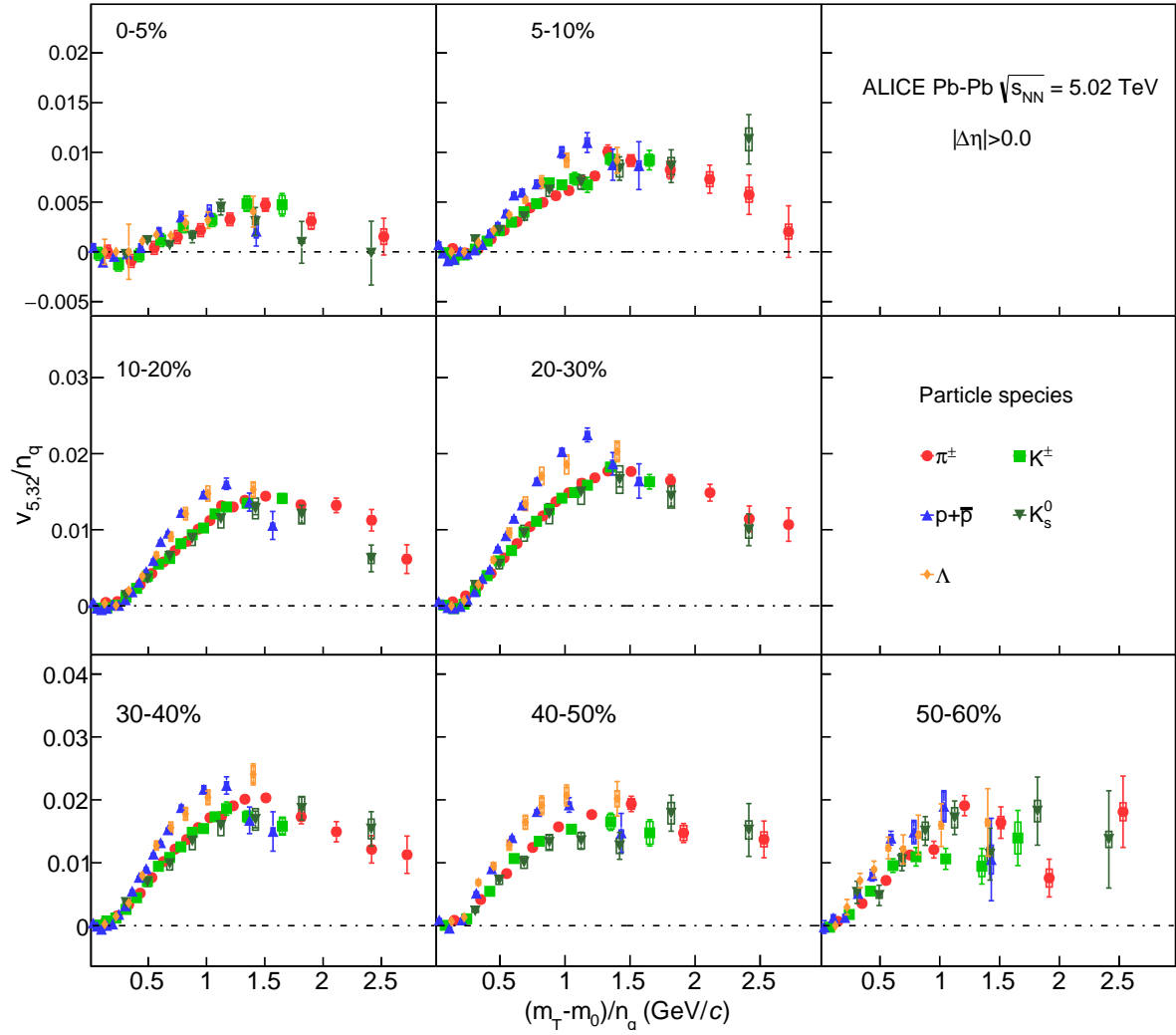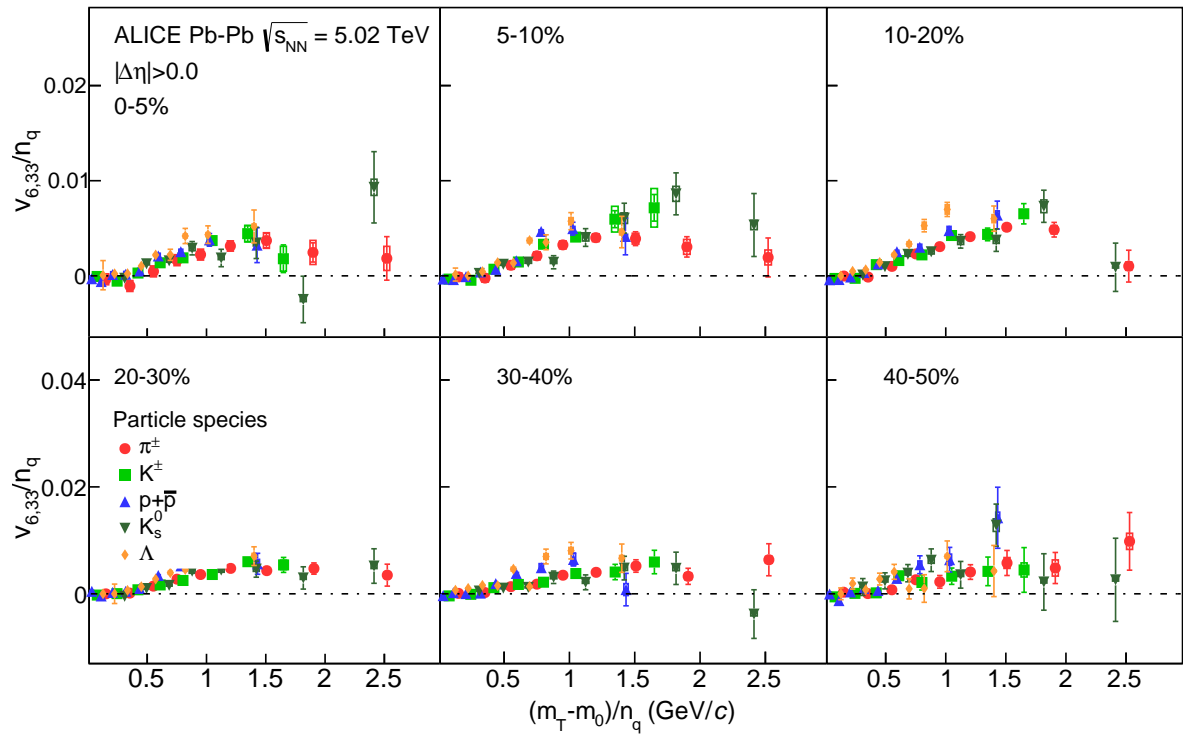
B   The ALICE Collaboration

Figure A.2: The $(m_T - m_0)/n_q$-dependence of $v_{5,32}/n_q$ for different particle species grouped into different centrality intervals of Pb–Pb collisions $\sqrt{s_{NN}} = 5.02$ TeV

Figure A.3: The $(m_T - m_0)/n_q$-dependence of $v_{6,33}/n_q$ for different particle species grouped into different centrality intervals of Pb–Pb collisions $\sqrt{s_{NN}} = 5.02$ TeV
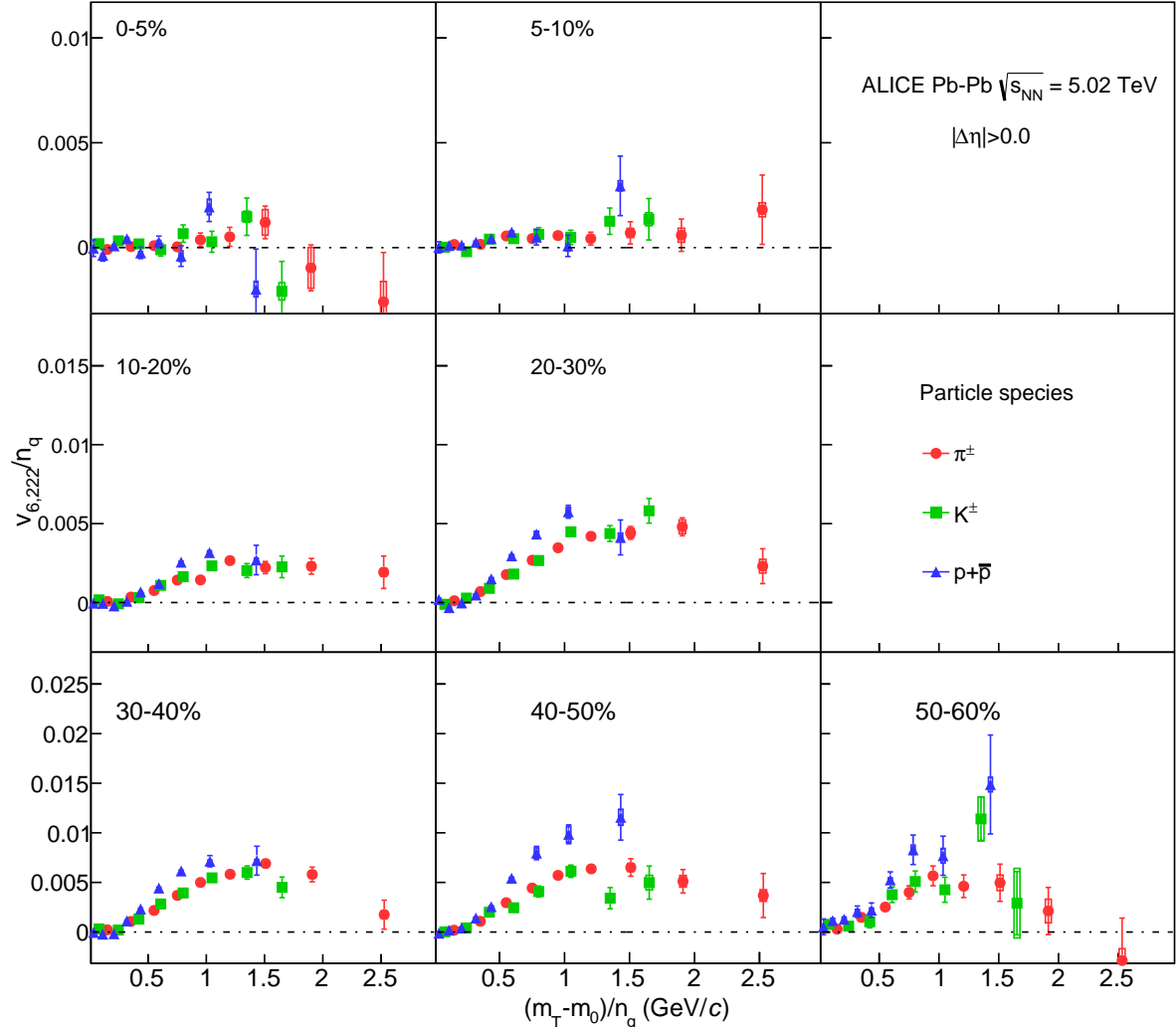
Figure A.4: The $(m_T - m_0)/n_q$-dependence of $v_{6,222}/n_q$ for different particle species grouped into different centrality intervals of Pb–Pb collisions $\sqrt{s_{NN}} = 5.02$ TeV